Carbon dioxide sources and sinks in the delta of the Paraíba do Sul River (Southeastern Brazil) modulated by carbonate thermodynamics, gas exchange and ecosystem metabolism during estuarine mixing

Luiz Cotovicz, Luciana Vidal, Carlos Eduardo de Rezende, Marcelo Bernardes, Bastiaan Knoppers, Rodrigo Sobrinho, Renan Cardoso, Marcelo Muniz, Roberto Meigikos dos Anjos, Antoine Biehler, et al.

▶ **To cite this version:**

Luiz Cotovicz, Luciana Vidal, Carlos Eduardo de Rezende, Marcelo Bernardes, Bastiaan Knoppers, et al.. Carbon dioxide sources and sinks in the delta of the Paraíba do Sul River (Southeastern Brazil) modulated by carbonate thermodynamics, gas exchange and ecosystem metabolism during estuarine mixing. Marine Chemistry, 2020, 226, pp.103869. 10.1016/j.marchem.2020.103869 . hal-02931519

HAL Id: hal-02931519
https://hal.science/hal-02931519

Submitted on 19 Oct 2021

HAL is a multi-disciplinary open access archive for the deposit and dissemination of scientific research documents, whether they are published or not. The documents may come from teaching and research institutions in France or abroad, or from public or private research centers.

L'archive ouverte pluridisciplinaire **HAL**, est destinée au dépôt et à la diffusion de documents scientifiques de niveau recherche, publiés ou non, émanant des établissements d'enseignement et de recherche français ou étrangers, des laboratoires publics ou privés.

Sources and sinks of CO_2 in the delta of the Paraíba do Sul River (Southeastern Brazil) modulated by carbonate thermodynamics, gas exchange and ecosystem metabolism during estuarine mixing

Luiz C. Cotovicz Jr.[a,b]; Luciana O. Vidal[c]; Carlos Eduardo de Rezende[c]; Marcelo C. Bernardes[a]; Bastiaan A. Knoppers[a]; Rodrigo L. Sobrinho[a]; Renan P. Cardoso[d]; Marcelo Muniz[d]; Roberto Meigikos dos Anjos[d]; Antoine Biehler[e]; Gwenaël Abril[a,f]

[a] Programa de Geoquímica, Universidade Federal Fluminense, Niterói, RJ, Brazil
[b] Instituto de Ciências do Mar (LABOMAR), Universidade Federal do Ceará, Fortaleza, CE, Brazil
[c] Laboratório de Ciências Ambientais, Centro de Biociências e Biotecnologia Universidade Estadual do Norte Fluminense, Campos dos Goytacazes, RJ, Brazil
[d] Laboratório de Radioecologia e Alterações Ambientais, Instituto de Física, Universidade Federal Fluminense, Niterói, RJ, Brazil
[e] Canada Research Chair in Geochemistry of Coastal Hydrogeosystems, Québec-Océan, Boreas Group on the North Systems, Université du Québec à Rimouski, Rimouski, Canada
[f] Biologie des Organismes et Ecosystèmes Aquatiques (BOREA), UMR 7208, Muséum National d'Histoire Naturelle, CNRS, IRD, SU, UCN, UA, Paris, France.

Corresponding author: Luiz C. Cotovicz Jr., lccjunior@id.uff.br

Marine Chemistry 226 (2020) 103869

https://doi.org/10.1016/j.marchem.2020.103869

Abstract

Tropical estuarine deltas generally present poorly buffered waters in their freshwaters. Carbonate chemistry predicts that mixture of such warm freshwater with seawater will create rapid consumption of the freshwater carbon dioxide (CO_2) by the carbonate buffering capacity of the seawater. In this study, we used the Paraiba do Sul River as a laboratory to investigate how thermodynamics compare with biological processes, gas exchange, and tidal advection from mangrove. We conducted three spatial surveys covering the salinity gradient of the main channel and surrounding mangrove waters and one 24-hour mooring in a mangrove creek. In the main channel, dissolved inorganic carbon (DIC) and total alkalinity (TA) showed closely conservative distribution along the salinity gradient, increasing seaward. The partial pressure of CO_2 (pCO_2) followed a bell-shaped curve predicted by carbonate chemistry for conservative mixing of river and ocean endmembers. During high river flow, pCO_2 sharply decreased between salinities 0 and 5 (1800 to 390 ppmv), a pCO_2 drawdown attributed to riverine outgassing and thermodynamics. Indeed, the mixing of TA-poor freshwater (363 $\pm$16 µmol kg^{-1}) with TA-rich seawater creates a deficit of dissolved CO_2 not related to biotic processes. During low river flow, the entire mixing zone was undersaturated in pCO_2 with an increasing trend seaward. However, observed pCO_2 values were slightly above those predicted by conservativity. Approximately half of this deviation was attributed to biological activity (net heterotrophy), and remaining deviation was assigned to the effects of gas exchange (18%) and water heating (36%). The effect of gas exchange was higher in fresh and low salinity waters, reflecting the higher outgassing/ingassing of CO_2, and lower buffering capacity. Water heating was more important in mid- to high-salinities as a result of diel patterns of solar irradiance. Heterotrophy was slight and not able to outcompete thermodynamics and generate outgassing during estuarine mixing. Consistently, stable isotopic signatures of DIC (δ^{13}C-DIC) presented slight deviations below the conservative mixing, corroborating net heterotrophy in the main channel. Areas of CO_2 uptake due to phytoplankton activity were identified but restricted to the freshwater endmember during low river flow, with lowest pCO_2 (up to 41 ppmv) and the highest chlorophyll *a* (up to 21.3 µg L^{-1}). The estuary was a CO_2 sink during low river flow (-1.34 to -5.26 mmolC m^{-2} d^{-1}) and a source during high river flow (5.71 to 19.37 mmolC m^{-2} d^{-1}). In the mangrove creek, the pCO_2, DIC, δ^{13}C-DIC and TA presented deviations from the conservativity, with slopes between TA and DIC demonstrating organic carbon degradation mediated by aerobic respiration and sulphate reduction. Mangrove creek waters were a CO_2 source (average of 134.81 mmolC m^{-2} d^{-1}), exhibiting high values of pCO_2 (up to 21,720 ppmv). The results reveal that the low buffering capacity in the main channel of tropical estuarine deltas can be the predominant driver of pCO_2, generating CO_2 undersaturation along the mixing zone, a process overlooked in estuarine systems. Moreover, air-water CO_2 exchange, thermal variability, and biological activities contribute to deviation of the carbonate system from conservative mixing in specific estuarine areas, also modulating pCO_2 variability.

Keywords: carbon dioxide, carbonate chemistry, thermodynamics, tropical coastal deltas

1. Introduction

The concentration of carbon dioxide (CO_2) in Earth's atmosphere has been increasing at fast rates, and the current CO_2 level is unprecedented over the past 3 million years (Willeit et al., 2019), changing approximately from 277 ppmv in 1750 (Joos and Spahni, 2008) to 414 ppmv in April 2019 (NOAA, 2018), as a result of fossil fuel burning and land-use changes. According to recent estimates, the oceans and the land absorb approximately 23 and 32% of these total emissions, respectively, whereas the remaining 45% accumulate in the atmosphere (Le Quéré et al., 2018). This CO_2 accumulation in the atmosphere is causing global warming, with CO_2 as the most important anthropogenic-derived greenhouse gas (IPCC, 2013). In addition, penetration of CO_2 in the ocean is causing acidification, increasing the surface ocean partial pressure of carbon dioxide (pCO_2), with a net decline of pH (Gattuso et al. 2015). While carbon sink in the open ocean is currently estimated with a relative high degree of confidence (2.5 ±0.5 GtC yr^{-1}; Le Quéré et al., 2018), the air-water CO_2 fluxes and controlling processes remain uncertain in the coastal ocean. Indeed, coastal oceans have not been satisfactory included in global carbon budget calculations, despite their importance in terms of global carbon cycling (Chen and Borges, 2009; Cai, 2011; Bauer et al., 2013).

Estuaries are aquatic ecosystems characterized by the mixing of fluvial and marine waters, hosting a large diversity of interfaces and gradients, with distinct physical, geomorphological and biological features (Cai, 2011; Borges and Abril, 2011). Studies have shown that CO_2 emissions by estuarine systems and near-shore coastal waters are globally significant (Chen and Borges, 2009). However, in 10 years of global data compilation, CO_2 emission estimates have decreased by a factor of 6. The first global estimate of estuarine CO_2 emissions calculated a degassing of 0.6 PgC yr^{-1} (Abril and Borges, 2004), whereas the two lasts estimates showed degassing of approximately 0.1 PgC yr^{-1} (Chen et al., 2013; Laruelle et al., 2013). This decline has been attributed to various factors, mainly the disproportional and insufficient global sampling (poor coverage in tropical regions and the Southern Hemisphere), few studies with direct and continuous measurements of pCO_2, and low temporal resolution (semi-diurnal, diurnal, seasonal, and annual) (Borges and Abril, 2011; Cai, 2011; Chen et al., 2013).

In general, the upper estuarine regions with low-salinity waters are important sources of CO_2 to the atmosphere. This is normally attributed their net heterotrophy and, to a lesser extent, to inputs of CO_2-enriched freshwater and lateral inputs from intertidal areas such as salt marshes and mangroves (Cai et al., 1999; 2011; Borges and Abril, 2011). However, in some estuaries, the riverine contributions of

CO_2 (allochthonous sources) can be greater than contribution of estuarine heterotrophy (autochthonous sources) at certain times of the year (Jiang et al., 2008; Joesoef et al., 2015; Van Dam et al., 2018a). Climatological and hydrological characteristics may change seasonally according to river water discharge, temperature, and formation of vertical stratification, which modulate physical mixing and biological production (Frankignoulle et al., 1998; Salisbury et al., 2008; Borges and Abril, 2011; Dinauer and Mucci, 2017). Downstream in the seaward direction, estuarine mixing zones are considered as moderate CO_2 sources, whereas the marine domain from the river mouth to the shelf break generally behaves as a CO_2 sink (Frankignoulle et al., 1998; Borges and Abril, 2011; Chen et al., 2013). In general, the pCO_2 values and CO_2 emissions are much higher in river-dominated estuaries than in marine-dominated estuaries (Jiang et al., 2008; Cotovicz et al., 2015). In addition to the marked and complex natural variability, the coastal ocean hosts approximately 37% of the human population (Cohen et al., 1997), creating human-induced modifications in the metabolism of aquatic ecosystems associated with nutrient enrichment and eutrophication (Frankignoulle et al., 1998; Zhai et al., 2007; Cotovicz et al., 2015; Kubo et al., 2017).

Historically, studies addressing estuaries have identified biological processes as predominant drivers on pCO_2 distribution and CO_2 fluxes along salinity gradients (Frankignoulle et al., 1998; Cai et al. 1999; Borges and Abril, 2011). However, the theory of carbonate chemistry predicts drastic abiotic changes in proportions of dissolved CO_2, bicarbonate (HCO_3^-), and carbonate (CO_3^{2-}) during the mixing of freshwater with seawater. The influence of thermodynamics in the CO_2 system in estuarine waters was first described by the pioneer studies of Mook and Koene (1975) and Whitfield and Turner (1986). These authors showed that modification of the carbonate equilibria in estuarine waters during the mixing of freshwater with seawater results in changes in the pCO_2 and, in turn, in the CO_2 fluxes at the air-water interface (Whitfield and Turner 1986; Hu and Cai, 2013; Cai et al., 2013). In particular, the displacement of acid-base equilibrium during the mixing of weakly buffered freshwater (low total TA concentration) with well buffered seawater (high TA concentration) can generate pCO_2 values far below that of the atmosphere, with no need for biological uptake (Whitfield and Turner 1986). In this regard, thermodynamic processes would be potentially significant compared with biological processes in oligotrophic/mesotrophic estuaries with short residence times as, for example, estuarine deltas. Thermodynamic changes as the main driver of carbonate chemistry changes along the salinity gradient in estuaries were have been demonstrated in theoretical studies (Hu and Cai, 2003; Salisbury, 2008; Cai et al., 2013), but rarely validated using field data. In the Amazon River plume, pCO_2 undersaturation has been attributed mainly to phytoplankton productivity (Ternon et al., 2000; Körtzinger, 2003); however, recent findings showed that, from a salinity value of approximately 10, surface water becomes undersaturated as a result of the mixing effect (Lefèvre et al., 2017).

The geographical position also exerts influence over CO_2 concentrations and emissions across different latitudes. Estuaries located at low and intermediate latitudes present the largest flux per unit

area, whereas those located in regions north of 50° N and south of 50° S present the lowest flux per unit area (Chen et al., 2013). These differences are attributed to local/regional characteristics of the coastal zone, including the mixing of freshwaters (presenting variable levels of pCO_2) with low-pCO_2 shelf waters, water temperature, and biogeochemistry complexity (Chen et al., 2013). However, it should be highlighted that studies on carbon cycling conducted in tropical coastal regions are overlooked compared with those in temperate and boreal regions. In addition, tropical rivers present lower TA concentrations than temperate/boreal rivers (Cai et al., 2008), thus the impact of thermodynamic processes during river-ocean mixing can be especially important in tropical estuaries. Estuarine deltas can locally/regionally be the main estuarine type through which significant terrestrial carbon is transported to the ocean (Laruelle et al., 2013). Deltas are mostly located in tropical and sub-tropical regions (Laruelle et al., 2013).

The present study aims at investigating the carbonate chemistry and air-water CO_2 exchange in the Paraiba do Sul River estuary (PSRE), southeastern Brazil. This estuary is a tropical mesotrophic ecosystem that has been suffering with increasing eutrophication and construction of dams in its watershed. This ecosystem has a short residence time and low TA concentrations in freshwater, potentially generating pCO_2 undersaturation conditions during mixing with seawater as a result of thermodynamic changes - a fact that is still disregarded globally. Based on high resolution monitoring of carbonate chemistry parameters along the entire salinity gradient, we could differentiate between the biotic and abiotic contributions to water pCO_2 distributions and CO_2 fluxes at the air-water interface; we also analyzed the metabolism of the main channel using pCO_2 distributions and stable isotope data.

2. Material and Methods

2.1 Study Area

The Paraiba do Sul River is an important water resource located in the southeast region of Brazil. The river watershed has an area of approximately 54,400 km^2, with a length of 1,145 Km, traversing the most industrialized and urbanized region of Brazil (the states of São Paulo, Minas Gerais and Rio de Janeiro). According to previous studies, the river basin is divided into three regions (Ovalle et al., 2013): 1. the upper basin (7,300 km^2), with water sources at 1,800 m of altitude until 600 m in a valley of crystalline rocks; 2. the medium basin (27,500 Km^2), with average elevation of 500 m; 3. the lower basin (22,500 km^2), comprising coastal plains, with extensive meanders and islands until the river mouth into the Atlantic Ocean (Fig. 1).

The PSRE, located at the north region of the state of Rio de Janeiro (21°37′ S; 41°01′ W), is composed of a main river channel and a minor secondary channel (Fig. 1). The secondary channel harbors a

mangrove forest of approximately 8 km^2 (Sterza and Fernandes, 2006). The coast is microtidal with high energy of waves, forming an estuarine delta. According to the Köppen's classification, climate in the region is Aw, with wet summers (November to January) and dry winters (July to September) (Cotovicz et al., 2013). The river discharge in the estuary follows a seasonal cycle, with high water flow in summer and early spring and low water flow in winter and early autumn, with discharges averages of 1158 and 444 $m^3 s^{-1}$, respectively. The river discharge modulates the residence time of waters in the mixing zone (Souza et al., 2010) and the extension of the river plume in the adjacent coastal ocean (Rudorff et al., 2011). During low water flow, the plume is reduced and it takes approximately 10 days for the water to reach open ocean (salinity 35), whereas during high water flow, the plume is extended along the shelf and the residence time decreases to 6 days (Souza et al., 2010).

The river has undergone increasing anthropogenic influences. The total human population on its watershed is estimated at 5 million inhabitants. Considering only the estuarine region, the surrounding population is estimated at approximately 600,000 inhabitants (IBGE, 2018). In addition, the lower basin presents extensive farming, particularly sugar cane production (Ovalle et al., 2013). The coverage of wastewater treatment plans is still very small in the region, less than 50% of the total households. Therefore, the estuary receives a large amount of industrial, agricultural and domestic effluents, with large inputs of nutrients to the waters, thus presenting mesotrophic characteristics (Cotovicz et al., 2013). Reservoirs and hydroelectric dams have been constructed along the drainage basin (forty-seven different hydroelectric power plants; Ovalle et al., 2013), which have changed hydrological patterns and potentially altered carbon cycling in the estuary.

2.2 Sampling Strategy

Three extensive spatial surveys were conducted in the estuary on February 17, October 17 and March 18. The Feb 17 sampling, historically considered as the rain season, presented an accumulated monthly precipitation of 40 mm, which is 60 mm lower than the historical average, with a 7-day accumulated precipitation before sampling of only 1 mm. The Oct 17 sampling presented an accumulated monthly precipitation of 13 mm (80 mm lower than the historical average), with a 7-day accumulated precipitation before sampling of 4 mm. The Mar 18 sampling presented an accumulated monthly precipitation of 376 mm, which is 267 mm higher than the historical data. Thus, the Feb 17 and Oct 17 samplings were considered dry conditions and the Mar 18 sampling was considered wet condition. These climatological characteristics influenced the hydrological pattern. The Feb 17 and Oct 17 samplings were conducted during low river flow, with average discharges of 288 and 178 $m^3 s^{-1}$, respectively (Fig. 1c,d), whereas the Mar 18 collection was performed during high river flow, with average discharge of 1,240 $m^3 s^{-1}$. The mean historical river water discharge (reference period of 95 years, 1923-2018) presented higher values than the discharge verified on the sampling days (Fig.

1c,d). The regression line of the historical data shows that the river discharge has been decreasing at a rate of ~5 $m^3 s^{-1}$ per year, which means that the mean discharge has already decreased by 475 $m^3 s^{-1}$.

In each sampling campaign, continuous and discrete aquatic measurements were performed. Continuous and online measurements were conducted for pCO_2, dissolved oxygen (DO), pH, salinity, and temperature. Surface water was sampled in the mangrove creeks and in the main channel in discrete points distributed regularly along the whole salinity gradient (0 to 35) with approximately three salinity unit increments. Discrete samples were used to analyze TA, Chl *a*, and δ^{13}C-DIC. The spatial surveys covered the freshwater domain (upper estuary), the mixing zone (complete salinity gradient), and the external estuary (river plume adjacent to the coastal ocean). The spatial surveys started in the morning, at around 8:30 am, and finished in the early-afternoon, at around 4:00 pm. In addition to the spatial survey screening, an Eulerian time series (24 h of sampling) was conducted in the mangrove tidal creek located in the secondary channel on March 2018 (Fig. 1), combining continuous measurements and discrete water sampling within 2 hours of interval for the same water parameters previously described.

2.3 Continuous Measurements

Continuous samplings were performed from a boat, with real-time measurements of position, pCO_2, DO, pH, salinity, and temperature, at a frequency of 1 min (Frankignoulle et al., 2001, Abril et al., 2014; Cotovicz et al., 2016). Briefly, a water pump placed at a depth of ~0.5 m provided continuous 6 L min^{-1} water flux to the boat. A part of this flux (~3 L min^{-1}) was directed to an equilibrator to measure the pCO_2. The marble equilibrator consisted of an acrylic tube (60 cm in length; 8 cm in diameter) filled with glass marbles where the water flows from top to bottom and a closed air circuit with a flow of ~1 L min^{-1} in the opposite direction, from bottom to top. The air is dried using a desiccant (Drierite™) and pumped into a non-dispersive infrared gas analyzer (Li-820 NDIR, LI-COR). Before and after each sampling campaign, the NDIR was calibrated using gas standards with air pCO_2 values of 410, 1007 and 5035 ppmv (White Martins Certified Material, RJ, Brazil). Fresh soda lime was used to set the zero and the standard at 1007 ppmv was used to set the span. The air standards of 1007 and 5035 ppmv were used to verify the system stability. The boat speed was 8-10 km h^{-1} during the spatial surveys. The equilibration time of the pCO_2 measurement system is 2-3 min (Cotovicz et al., 2016). This gas equilibration device is ideal for pCO_2 analysis in estuarine waters due to its fast response time (Frankignoulle et al., 2001, Abril et al., 2014; Cotovicz et al., 2016). This time is sufficient to guarantee the equilibration along the estuarine mixing. In the steepest part of the salinity gradient, between salinities 10 and 20, the velocity of the vessel was reduced to less than 2 km h^{-1} before all discrete sampling, this allowed a complete gas equilibration for pCO_2 measurements. Accuracy of the pCO_2 measurements was estimated at ±5 ppmv. Temperature, salinity, and DO were

measured using a calibrated YSI Professional Plus multiparameter meter, and pH was measured using a WTW 3310 pH meter equipped with a Sentix 41 electrode, calibrated with a three-point standard (pH 4.01, pH 7.00 and pH 10.01) according to the National Institute of Standards and Technology (NIST), before and after each sampling campaign. The precision of the pH measurements estimated after seven verifications against standards before and after each sampling campaign was approximately 0.01 NBS units. For the anchored continuous sampling (Eulerian approach), the total duration of sampling was 20 h, encompassing one complete tidal cycle plus one ebb tide period. Two tidal cycles of measurements were not completed due to logistic problems.

2.4 Discrete Measurements and Laboratory Analysis

Discrete samples were collected at a depth of ~0.5 m using a Niskin bottle and then stored for further laboratory chemical analysis (i.e., fixed and/or kept on ice in the dark). The water was filtered with Whatman® grade GF/F glass microfiber filters (pre-combusted at 500 °C for 6 h), followed by determination of TA and Chl *a*. The filters used to analyzed Chl *a* were kept at −18 °C prior to analysis. TA measurements were performed according to the classical Gran (1952) titration in an automated titration system (Metler Toledo model T50) in filtered water samples. The accuracy of this method was better than ±5 μmol kg^{-1} (inferred from certified reference material - CRM; A. G. Dickson from Scripps Institution of Oceanography). Chl *a* was extracted from the filters with 90% acetone and quantified by spectrophotometry according to Strickland and Parsons (1972). For δ^{13}C-DIC measurement, water was sampled and transferred directly to 150 mL serum vials, which were poisoned by adding 0.2 mL of a $HgCl_2$ saturated solution, and then sealed. In the laboratory, δ^{13}C-DIC was determined following the protocol by Bouillon et al. (2007). A headspace of approximately 40 mL was created with Helium, and 0.2 mL of ultrapure concentrated H_3PO_4 was introduced to convert all inorganic carbon to CO_2. The samples were shaken and kept in the dark at controlled temperature of 25 °C for 12 h. The δ^{13}C of CO_2 in the headspace was determined by injecting 0.5-1 mL of headspace gas in an isotopic ratio mass spectrometer (IRMS) equipped with a manual gas injection port. δ^{13}C-DIC was calibrated using laboratory standards, which were prepared by adding 45 mg of Na_2CO_3 in a sealed vial flushed with helium and dissolved with 3 mL of 85% H_3PO_4, as described in Deirmendjian and Abril (2018). This standard was calibrated against a certified standard (NBS 19, -1.96‰) using a dual-inlet IRMS. The isotopic value of the Na_2CO_3 standard was -4.5 ±0.2‰. The obtained δ^{13}C values were corrected for the partitioning of CO_2 between the gaseous (headspace) and water phases in each sample using the algorithm of Miyajima et al. (1995). Repeatability of the analysis was ~0.1‰. The δ^{13}C-DIC concentrations are reported in ‰ relative to the standard Vienna Pee Dee Belemnite (V-PDB) scale.

2.5 Calculations

2.5.1 Carbonate System

DIC was calculated from pCO_2, TA, temperature, and salinity using the CO2calc 1.2.9 program (Robbins et al., 2010). We used the dissociation constants for carbonic acid proposed by Mehrbach et al. (1973) refitted by Dickson and Millero (1987), the borate acidity constant from Lee et al. (2010), the dissociation constant for the HSO_4^- ions from Dickson (1990) and the CO_2 solubility coefficient of Weiss (1974). The estimated uncertainty was better than ± 6 µmol kg^{-1} for DIC (Orr et al., 2018).

2.5.2 Excess DIC (E-DIC) and Apparent Utilization of Oxygen (AOU)

The excess of DIC (E-DIC, µmol kg^{-1}) was calculated according to Abril et al., (2003):

$$E\text{-}DIC = DIC_{sample} - DIC_{equilibrium} \quad (1)$$

Where DIC_{sample} represents the measured concentration of DIC (µmol kg^{-1}) and $DIC_{equilibrium}$ is the theoretical DIC at atmospheric equilibrium (µmol kg^{-1}). $DIC_{equilibrium}$ was calculated from the observed TA and the measured atmospheric pCO_2 during the cruises.

The apparent oxygen utilization (AOU, µmol kg^{-1}) was calculated as proposed by Benson and Krause (1984):

$$AOU = DO_{equilibrium} - DO_{sample} \quad (2)$$

Where DO_{sample} is the measured DO, and $DO_{equilibrium}$ is the DO saturation.

2.5.4 Diffusive air-water CO_2 fluxes

Diffusive fluxes of CO_2 at the air-water interface were calculated according to the following equation:

$$FCO_2 = k_{CO2,T} \cdot k_0 \cdot \Delta pCO_2 \quad (3)$$

Where FCO_2 is the diffusive flux of CO_2, $k_{CO2,T}$ is the gas transfer velocity of CO_2 at a given temperature (T), k_0 is the solubility coefficient of CO_2 calculated from in situ temperature and salinity (Weiss, 1974), and the ΔpCO_2 is the difference between the measured water pCO_2 and the measured atmospheric pCO_2 . The atmospheric pCO_2 was measured every sampling day at morning, noon and afternoon. The gas transfer velocity of CO_2 $k_{CO2,T}$ was computed as follows (Jähne et al. 1987):

$$k_{CO2,T} = k_{600} \times (600/Sc_{CO2,T})^n \quad (4)$$

where k_{600} is the gas transfer velocity normalized to a Schmidt number of 600 (Sc = 600 for CO_2 at 20°C), $Sc_{CO2,T}$ is the Schmidt number of CO_2 at a given temperature (Wanninkhof, 1992), and n being equal to 2/3 for wind speed <3.7 m s^{-1} and equal to 0.5 for higher wind speed (Jähne et al., 1987; Guérin et al., 2007).

To compute the k_{600} values, we used three different parameterizations proposed by Wanninkhof (1992), Raymond and Cole (2001) and Abril et al. (2009), according to respectively:

$k_{600}(W92) = 0.31(U10^2)$ (5)

$k_{600}(RC01) = 1.91exp0.35U10$ (6)

$k_{600}(A09) = 1.80exp-0.0165v + [1.23 + 1.00LOG(S)]U10$ (7)

where k_{600} is the gas transfer velocity normalized to a Schmidt number of 600 expressed in cm h^{-1}, v is the water current velocity in m s^{-1}, S is the surface area of the specific estuarine section considered in km^2, and U10 is the wind speed at 10m height in m s^{-1}. Water-to-air CO_2 fluxes were calculated using the daily-average pCO_2 for each estuarine domain: low salinity domain (salinities 0-5), mixing domain (salinities 5-25), marine domain (salinities > 25), and mangrove domain. We also differentiated the gas transfer velocities at different moments (morning, afternoon and nighttime). We divided the gas transfer velocities for these periods because the region is strongly impacted by marine breezes, wind speed being stronger during midday/afternoon than during the night/early morning (Amarante et al., 2002; Cotovicz et al., 2015). Wind speed wind velocity (U10), accumulated precipitation and atmospheric temperature were recorded in the meteorological station of Campos dos Goytacazes City and were provided by the National Institute for Space Research (INPE). The water current velocities were taken from Ovalle et al. (2013).

Rudorff et al. (2011) calculated the spatial coverage of the Paraiba do Sul River plume applying a spectral linear mixture analysis. The authors proposed a linear regression to estimate the surface area of the estuarine plume in the coast as a function of the historical river discharge. We applied this general linear regression to estimate the river plume spatial coverage for our sampling period of maximal river discharge (Mar-18), when the river discharge averaged 1,240 m^3 s^{-1}, and the extension of river plume was calculated at about 90.75 km^2. Accounting for the salinity values along the boat's trajectories, we constructed maps of surface salinity applying the data-interpolating variational analysis (DIVA gridding) using the Ocean Data View Software. The spatial coverages of the salinity zones for each sampling campaign were used to calculate the area-averaged CO_2 flux (Fig. S1, Supplementary file).

2.5.5 Mixing Models

Two types of mixing models were applied, one for TA, DIC and δ^{13}C-DIC in the discrete samples, and one for temperature, salinity and pCO_2, which were recorded continuously.

For DIC and TA, the model assumes conservative mixing according to

$C_{mix} = C_{freshwater}C_{freshwater} + C_{marine}(1 - C_{freshwater})$ (8)

Where C_{mix} is the concentration of a given solute during conservative mixing (in our case TA and DIC), and the subscripts freshwater and marine indicate the endmember concentrations in the river and the ocean, respectively. The freshwater fraction ($F_{freshwater}$) is calculated as:

$$F_{freshwater} = 1 - sal_{sample}/sal_{marine} \quad (9)$$

Where sal refer to the salinity, and the subscript sample refers to the *in situ* values for each station.

Concerning stable isotope ratios, we calculated the conservative mixing of δ^{13}C-DIC (δ^{13}C-DIC$_{mix}$) according to Mook and Tan (1991), as follows:

$$\delta^{13}C\text{-}DIC_{mix} = sal_{sample}(DIC_{freshwater}\delta^{13}C_{freshwater} - DIC_{marine}\delta^{13}C_{marine}) + sal_{freshwater}DIC_{marine}\delta^{13}C_{marine} - Sal_{marine}DIC_{freshwater}\delta^{13}C_{freshwater} / sal_{sample}(DIC_{freshwater} - DIC_{marine}) + sal_{freshwater}DIC_{marine} - sal_{marine}DIC_{freshwater} \quad (10)$$

Where δ^{13}C is the isotopic signature of DIC, the subscripts freshwater and marine indicate the endmember concentrations in the river and the ocean, respectively, and the subscript sample indicate the in situ values at each station.

The TA and DIC concentrations measured in the discrete samples (see result section) were close to the conservative mixing line. Thus we could compute these two parameters for each salinity obtained with the continuous measurements. The theoretical pCO_2 conservative mixing curve ($pCO_{2mixing}$) was obtained by solving the carbonate system using the in situ temperature and salinity, and the computed conservative TA and DIC for each salinity value obtained with the continuous measurements from the estuary (Jiang et al. 2008; Joesoef et al., 2015). Because the pCO_2 was variable in the freshwater endmember, we calculate the average and standard deviations for each sampling campaign.

In order to allow a full comparison with the observed pCO_2 distribution, two corrections of the conservative mixing pCO_2 model are necessary: a correction for gas exchange and another for the effect of heating or cooling in the estuary. In order to correct the mixing pCO_2 curve for gas exchange, an iterative calculation was applied for each salinity increment. The loss or gain of DIC as CO_2 evasion or invasion between each salinity increment "sal" was calculated as:

$$DICgain(sal) = -FCO_2(sal).RT.H^{-1} \quad (11)$$

Where FCO_2(sal) is the flux (mol m^{-2} h^{-1}) for every salinity unit, RT is the residence time (h) during mixing between salinity (sal) and (sal+1) and H is the water depth (m). FCO_2(sal) is calculated with Eq.3, and the conservative mixing pCO_2 (sal). The new corrected DIC concentration at sal+1 is obtained by adding the DICgain(sal+1) to the DIC(sal+1) previously deduced from the conservative mixing of DIC(sal) with DIC$_{marine}$:

$$Corrected\ DIC(sal+1) = DIC(sal+1) + DICgain(sal) \quad (12)$$

Then we recalculate the corrected pCO_2(sal+1) from a new mixing lines between corrected DIC(sal+1) and DIC$_{marine}$, and TA(sal+1) and TA$_{marine}$. The next iteration consisted in calculating the FCO_2(sal+1) from the corrected pCO_2(n+1) and the DICgain(sal+2) using Eq.3. The difference between $pCO_{2gas\ exchange}$ and $pCO_{2mixing}$ ($\Delta pCO_{2gas\ exchange}$) is attributed to gas exchange.

374 The thermal influence on the pCO_2 (cooling or heating), was calculated from the TA and DIC
375 conservative mixing, and this time by considering not the in situ measured temperature, but the
376 temperature calculated as linearly conservative between the two endmembers. The difference between
377 $pCO_{2mixing}$ (calculated with in situ temperature) and the pCO_2 calculated with the endmembers
378 interpolation is attributed to the thermal pCO_2 along the mixing zone ($\Delta pCO_{2cooling/heating}$).

379 2.6 Statistical analysis

380 We applied the Shapiro–Wilk test to investigate the normality of the data set. As the data did not
381 follow normal distributions, we applied non-parametric statistics. To compare the differences between
382 averages for the concentrations of biogeochemical parameters in water, we applied the Mann–Whitney
383 test, which compares the distributions of unmatched groups. Linear and non-linear regressions were
384 calculated to analyze the correlations between variables, providing the best-fit slope, the intercept and
385 the goodness of fit (R^2). All statistical analyses were based on $\alpha = 0.05$. The statistical tests and
386 calculations were performed with the Graph Pad Prism 6 program.

387 **3. Results**

388 3.1 Spatial and temporal variations of carbonate chemistry and ancillary parameters

389 Spatial and temporal variations of pCO_2 and the main parameters analyzed in this study are presented
390 in Table 1 for the four domains. Surface water temperature showed a marked seasonal trend between
391 26.2 and 31.8 °C in summer (Feb 17 and Mar 18 samplings) and between 23.4 and 26.2 °C in winter
392 (Oct 2017 sampling). The highest temperatures were found in freshwaters, with a cooling trend
393 seaward. This decrease in water temperature was slight, with less than 2 °C difference, on average,
394 between the river and marine zones. However, this seaward temperature decrease trend was not linear
395 during estuarine mixing. Intermediate salinities (values from 20 to 30) were generally sampled close to
396 midday, when the solar irradiance is maximum. These intermediate salinities exhibited temperatures
397 higher than that expected for the conservative mixing because of the heating effect (>0.8 °C, on
398 average), reaching 2.2 °C during sampling on March 18. In contrast, waters with temperatures lower
399 than that expected for the conservative mixing (cooling effect) were verified only on the Feb 17
400 sampling in low salinities.

401 The spatiotemporal salinity distribution in surface waters was governed by the river water discharge
402 (Fig. 2; Fig. S1 Supplementary information). This figure shows the boat track for the three sampling
403 campaigns. Note that the boat tracking was not the same for the sampling campaigns. The principal
404 reason for these differences is that the main estuarine channel navigated in the first two trips (Feb 17
405 and Oct 17) became very shallow and dangerous for navigation. For safety reasons, we decided to
406 navigate along the secondary channel during the trip of March 18. During the period of lowest
407 freshwater discharge (178 $m^3 s^{-1}$), the mixing zone was located close to the river mouth, with an

intrusion of brackish water (salinity ≤20) until approximately 4 km inside the internal estuary at high tide. Consequently, at low river discharge, the river plume covered a small area (~30 km^2) in the adjacent shelf waters, with the marine zone (salinity >30) located closest to the river mouth (between 3 and 6 km from the river mouth) (Fig. S1). Contrastingly, during the Mar 18 sampling at high river flow (1,240 m^3 s^{-1}), the mixing zone was located outside the limit of the coast, and no salinity intrusion occurred in the internal estuary (Fig. 2c). During this high flow period, the mixing zone covered the highest surface area (~63 km^2) in the adjacent shelf (extending to approximately 12 km from the river mouth), with the marine zone located far from the internal estuary (>10 km) (Fig. S1).

Surface water pCO_2 in the estuary was strongly related to the salinity and followed a distribution close to that predicted for the mixing curve between the river and marine endmembers, with marked differences between the dry and rainy seasons in the low salinity region (Figs. 2 and 3). During low river flow, the low salinity regions (0-5) presented undersaturated pCO_2 conditions compared with the equilibrium with atmosphere in all sampling campaigns, with mean values of 157 ±47 ppmv and 192 ±52 ppmv for the Feb 17 and Oct 17 samplings, respectively (Fig. 2a,b). In the seaward direction, pCO_2 increased with salinity, following a general trend close to the thermodynamic mixing curve (Figs. 2a,b and 3a,b). During the rainy period, the river zone presented high pCO_2 values with permanent oversaturation (mean of 1,946 ±252 ppmv). However, pCO_2 showed a sharp decline between salinities 0 and 5, and quickly reached undersaturated conditions at salinity higher than ~10, with a mean value of 380 ±116 ppmv in the mixing zone (Fig. 2l and 3h). The marine zone (salinity >30), during the rainy period, showed pCO_2 values close to those found during the dry period, 439 ±17 ppmv, on average. Mangrove-dominated waters (mangrove creek) presented pCO_2 values much higher (up to 11,514 ppmv) than that found in the waters of the main estuarine channel in all sampling campaigns.

Strong relationships with salinity were also verified for carbonate chemistry parameters, including TA, DIC, and δ^{13}C-DIC (Fig. 4). The TA and DIC concentrations for the freshwater endmember presented small but statistically significant seasonal variation depending on the intensity of river flow (Mann–Whitney test, $p<0.0001$). The TA and DIC concentrations in the freshwater endmember were 446 ±89 (n = 4) and 435 ±77 µmol kg^{-1} (n = 3) during the dry season and 428 ±101 and 469 ±86 µmol kg^{-1} during the wet season (n = 4), respectively. In the mangrove waters, the TA and DIC concentrations were much higher than those in the conservative mixing, and did not follow the linear pattern found in the main channel (Fig. 4a,b,c,d,e,f). Concerning the δ^{13}C-DIC signatures, the freshwater endmember showed important seasonal variation according to river discharge (Fig. 4). During low river flow (Feb 17 and Oct 17 samplings), freshwater δ^{13}C-DIC values showed a mean of -3.55 ±0.43‰, and the distributions along the salinity gradient showed slight ^{13}C depletion compared with the conservative mixing curve (Fig. 4). During high river flow, the stable isotope signature mean was -7.38 ±1.49 ‰, and the δ^{13}C-DIC distributions along the salinity gradient showed only a minor deviation from the

conservative mixing curve. δ^{13}C-DIC values in the mangrove creek were more negative than in the main channel during the two dry periods assessed, with mean and minimum values of -10.96 ±1.23‰ and -11.82‰, respectively (Fig 4g,h). During the rainy period, the δ^{13}C-DIC values in the mangrove creek presented a mean of -6.43 ±1.79‰, with enrichment in ^{13}C compared with that of the waters of the main channel, and above the conservative mixing curve (Fig. 4i).

During the dry period, Chl *a* concentrations were higher in freshwaters (between 3.86 and 21.30 µg L^{-1}) and showed a marked decrease in the seaward direction (Fig. 4j,k). This decrease in Chl *a* concentrations with increasing salinity is coincident with an increase in pCO_2. Chl *a* and pCO_2 were negatively correlated in the main channel (R^2 = 0.59 on Feb 17; R^2 = 0.60 on Oct 17; p<0.001) (Fig. 5). On the other hand, for the rainy period, the freshwaters presented the lowest Chl *a* concentrations, and the distributions did not follow a clear pattern along the salinity gradient, not presenting significant correlations with pCO_2 (Figs. 4 and 5). The Chl *a* concentrations in the mangrove tidal creek were high for all the sampling campaigns, reaching a maximum value of 26 µg L^{-1} on February 17.

3.2 Tidal and diurnal variations of carbonate chemistry in the mangrove creek

Results of diurnal variations of the carbonate chemistry parameters in the tidal creek are presented in Table 2 and Figures 6 and 7. We sampled one ebb tide at daytime followed by one flood tide at nighttime and one ebb tide at nighttime. Tidal amplitude was 0.42 m for the first ebb phase (from ~12:00 pm to 06:30 pm) and 0.64 m for the second ebb phase (from ~00:30 am to 07:30 am). For the first tidal cycle, no statistically significant difference was observed between the ebb and flood tides (Mann Whitney Test; p>0.05); however, the second ebb tide (nighttime) presented higher salinity values than those found in the other sampled periods (Mann Whitney Test; p<0.01), following an atypical pattern. Daytime sampling presented higher average temperature (30.0 ±0.3 °C) than nighttime sampling (28.3 ±0.3 °C).

In the mangrove creek, pCO_2 values varied drastically along the diurnal time scale, with means of 7,439 ±1,390 ppmv during daytime ebb tide, 11,191 ±2,264 ppmv during nighttime flood tide, and 18,276 ±3,408 ppmv during nighttime ebb tide (Table 2). The maximum pCO_2 value (21,720 ppmv) occurred during nighttime ebb tide, whereas the minimum pCO_2 value (5,318 ppmv) occurred during daytime ebb tide. The highest pCO_2 values during nighttime ebb tide were coincident with the highest TA, DIC and salinity concentrations and the lowest pH and δ^{13}C-DIC values (Figs. 6 and 7). In this way, pCO_2 showed strong negative correlations with DO (R^2 = 0.99; p<0.0001) and δ^{13}C-DIC (R^2 = 0.97; p<0.0001) (Fig. 7d). Hypoxic and anoxic conditions occurred from the end of the nighttime period until sunrise (between approximately 00:30 am and 07:30 am) (Fig. 6c). DO concentrations were also strongly positively correlated with δ^{13}C-DIC values (R^2 = 0.96; p<0.0001) (Fig. 7c). During the diurnal cycle in the mangrove creek, δ^{13}C-DIC values varied between -8.79‰ (nighttime ebb tide) and -3.27‰ (daytime flood tide). The TA and DIC distributions followed a nearly linear relationship

with salinity (Fig. 7a). Increased TA concentrations followed decreased DO concentrations linearly, but only under hypoxic/anoxic conditions (Fig. 7b). As expected, E-DIC and AOU were well correlated in the mangrove creek, presenting positive concentrations and a high deviation above the line 1:1 in all sampling campaigns, which were different from the main channel pattern (Fig. 8a). The TA and DIC concentrations also showed strong deviation from the conservative mixing (ΔTA and ΔDIC), and different from the pattern observed in the main channel (Fig. 8b).

3.3 Gas transfer velocities and CO_2 exchanges at the air-water interface

The *k*-wind speed parameterization is one of the most critical parameters to compute the air-sea CO_2 fluxes between the pCO_2 gradients in the surface ocean and lower atmosphere (Borges and Abril, 2011; Wanninkhof, 2014; Call et al., 2015). Diverse formulations of *k*-wind parameterizations are available to estimate the main driving forces of turbulence at the air-sea interface, based on theoretical results from several studies that showed that their performance is more appropriate under certain conditions and environments (Wanninkhof, 2014). Thus, we computed the air-sea CO_2 fluxes using three different *k*-wind parameterizations: two appropriate for estuarine environments (Raymond and Cole, 2001; Abril et al., 2009) and one appropriate for open ocean waters (Wanninkhof, 1992), providing ranges of estimates (Table 3).

The calculated gas transfer velocities varied between 0.44 and 21.26 cm h^{-1} over the morning, afternoon and night periods (Table 3). The k_{600} values calculated from the equation of Abril et al. (2009) for estuarine waters, which account for wind velocity, estuarine size and current velocity, were higher than those calculated using the parameterizations proposed by Raymond and Cole (2001) and Wanninkhof (1992), except for wind speeds >6 m s^{-1}, when the equation of Abril et al. (2009) provided lower gas transfer values. The inner estuary current velocities estimated for each estuarine region, considering the water discharge and the cross-sectional area, ranged from 0.1 m s^{-1}, during low river flow, to 1.2 m s^{-1}, during high river flow. For the outer estuary (river plume), the current velocities were measured according to Knoppers et al. (1999). The Oct 17 sampling presented higher gas transfer velocity values compared with those measured on February 17 and March 18 (p<0.0001; t test) as a result of the higher wind speed averages. Higher computed gas transfer velocities occurred during the afternoon, followed by night and morning (Table 3).

Calculated CO_2 fluxes showed high spatiotemporal variability (Table 3) related to salinity and distance from the mangrove forest. The freshwater endmember was a CO_2 sink during low discharge and a CO_2 source during high discharge. The highest values of air-water CO_2 uptake in the estuarine zone (between -26.23 and -37.80 mmol C m^2 d^{-1}) were found during the afternoon, when wind speed was strongest. The mixing zone was also a CO_2 sink, but with smaller intensity compared with fresh and low-salinity waters. The air-water CO_2 fluxes in the mixing zone varied between -0.34 and -18.41 mmol C m^2 d^{-1}. The marine zone acted as a slight CO_2 source, with emissions ranging from 0.12 to

514 5.78 mmol C m^2 d^{-1}. The mangrove creek waters were a strong CO_2 source, with values ranging from
515 1.97 to 216.14 mmol C m^2 d^{-1}.

516 Considering all the estuarine areas and time of sampling (morning, afternoon and night), the estuary
517 was a slight CO_2 sink under dry conditions, with weighted surface fluxes ranging from -1.34 to -5.26
518 mmol C m^2 d^{-1} (Table 3), representing an uptake between 1.45 and 5.72 t C d^{-1}. During high river
519 discharge (Mar 18), the low salinity region was a strong CO_2 source, with emissions ranging from 6.36
520 to 117.77 mmol C m^2 d^{-1}, but the mixing zone remained a slight CO_2 sink, with fluxes varying
521 between -0.12 and -2.93 mmol m^2 d^{-1}. The marine zone was a CO_2 source, but with pCO_2 values very
522 close to the equilibrium with the atmosphere and emissions ranging from 0.05 to 1.27 mmol m^2 d^{-1}.
523 The mangrove tidal creek was a strong source of atmospheric CO_2, with degassing ranging from 9.34
524 to 358.39 mmol m^2 d^{-1}. Considering the estuary as a whole, the weighted CO_2 surface emissions during
525 high river discharge ranged from 5.71 to 19.37 mmol C m^2 d^{-1}, representing an efflux between 6.21
526 and 21.09 t C d^{-1}.

527 The riverine inputs of DIC to the estuary calculated by multiplying the DIC concentrations at the river
528 endmember by the river flow were 106 tC d^{-1}, 64 tC d^{-1} and 488 tC d^{-1} for the samplings conducted on
529 February 17, October 17 and March 18, respectively. Considering the estuary as a whole, the mean net
530 estuarine fluxes at the air-sea interface were -3.32 tC d^{-1}, -5.72 tC d^{-1} and 15.88 tC d^{-1} for the Feb 17,
531 Oct 17 and Mar 18 samplings, respectively. Consequently, the DIC inputs from the river to the estuary
532 were between ~11 and 32 times higher than the carbon influx or efflux at the air-water interface.

533 **4. Discussion**

534 4.1. Predominance of thermodynamic processes on pCO_2 distributions in the main channel and CO_2
535 air-water fluxes

536 Oversaturated pCO_2 conditions are usually observed in river-dominated estuaries as a result of the net
537 heterotrophic metabolism sustained by inputs of organic carbon from the catchment (Frankignoulle et
538 al., 1998; Dai et al., 2009; Cai, 2011; Borges and Abril, 2011), river input of dissolved CO_2 (Abril et
539 al. 2000; Jiang et al., 2008; Joesoef et al., 2015; Van Dam et al., 2018a), and of tidal pumping (Maher
540 et al., 2015; Santos et al., 2018). The overall trend of pCO_2 decreasing seaward has mostly been
541 described in rivers with moderate to high TA concentrations (≥1000 μmol kg^{-1}) and moderate to long
542 water residence time (Frankignoulle et al., 1998; Borges and Abril, 2011). However, in the case of
543 many tropical river deltas, TA concentrations are generally low at the riverine endmember (Cai et al.,
544 2008), and these estuaries have relatively short water residence time (Ludwig et al., 1998). Under such
545 conditions, thermodynamic changes during estuarine mixing generate strong pCO_2 undersaturation in
546 the low salinity region (Whitfield and Turner, 1986; Cai et al., 2013) that can exceed CO_2 production
547 and consumption by biological processes. Low TA concentrations in the river endmember provide low
548 buffering capacity in fresh and low salinity waters (Egleston et al., 2010; Hu and Cai, 2013; Cai et al.,

549 2013). We calculated the Revelle factor ($\gamma DIC = \partial \ln(CO_2)/\partial DIC)^{-1}$ along the mixing zone of the PSRE
550 to investigate its buffering capacity (Revelle and Suess, 1957; Egleston et al., 2010). The results
551 corroborate this hypothesis, showing that waters with salinities <10 presented the lowest buffering
552 capacity in all sampling campaigns (Fig. S2; Supplementary information).

553 In the PSRE, pCO_2 distributions along the salinity gradient were very close to that predicted by
554 theoretical thermodynamic changes during conservative mixing between the river and marine
555 endmembers, including a pCO_2 minimum much lower than the atmospheric value (Fig. 3). During low
556 river discharge (Feb-17 and Oct-17), the river endmember already presented CO_2 undersaturation with
557 relation to the atmosphere (due to phytoplankton uptake). During high river flow, pCO_2 was high in
558 freshwater, but showed a sharp decrease between salinities 0 and 5 and remained below the
559 atmospheric value along the mixing zone (salinity 0-30). This marked pCO_2 decrease occurred in
560 poorly buffered estuarine waters. The mixing of river water and seawater generates strong equilibrium
561 displacements between species of the carbonate system and strongly alters water pCO_2 values and air-
562 water CO_2 fluxes, creating pCO_2 undersaturation by inorganic processes (Whitfield and Turner, 1986;
563 Cai et al., 2013). In the case of acidic freshwater with low TA and eventually high pCO_2, dissolved
564 CO_2 is absorbed by the buffering capacity of the seawater and immediately incorporated into the
565 HCO_3^- and CO_3^{2-} pools rather than totally emitted to the atmosphere. Because the displacement of
566 chemical equilibriums is an almost instantaneous process, it can occur completely even with the short
567 residence time of waters of few days in the estuary.

568 A previous study discussed these acid-base processes in a theoretically, suggesting that the Amazon
569 River presents a CO_2 deficit along its mixing zone with relation to atmospheric conditions as a result
570 of thermodynamic changes, and the pCO_2 variations are quickly dominated by seawater, sustaining a
571 CO_2 sink along the river-ocean mixing (Cai et al., 2013). In the PSRE, these acid-base processes are
572 confirmed along the mixing zone, showing strong agreement between the theoretical model and *in situ*
573 data. For the three sampling campaigns, however, the pCO_2 values in the salinity gradient remained
574 close but slightly above the theoretical dilution curve ($pCO_{2\ mixing}$). The slight deviations of measured
575 pCO_2 compared with $pCO_{2\ mixing}$ are attributed to the influence of biological activities, gas exchange,
576 and thermal variability during estuarine mixing, as discussed in the following section.

577

578 4.2 Origin of the observed pCO_2 deviation from conservative mixing

579 Deviations of measured pCO_2 compared with $pCO_{2\ mixing}$ are potentially related to gas exchange,
580 thermal effect (heating/cooling), and ecosystem metabolism (estuarine autotrophy/heterotrophy plus
581 tidal pumping) during estuarine mixing (Jiang et al., 2008; Joesoef et al., 2015; Van Dam et al.,
582 2018a). In order to account for these processes, first we binned the measured pCO_2, calculating the
583 means and standard deviations for each salinity increment. Then we calculated the effects of gas

584 exchange and thermal variability on $pCO_{2\ mixing}$ as described in material and methods (section 2.5.5)
585 for the same salinity intervals, assuming a constant and homogeneous residence time along the entire
586 salinity gradient. This way we could calculate different pCO_2 curves during estuarine mixing:
587 measured pCO_2 ($pCO_{2\ measured}$), conservative pCO_2 ($pCO_{2\ mixing}$), conservative pCO_2 corrected for gas
588 exchange ($pCO_{2\ gas\ exchange}$), and conservative pCO_2 corrected for thermal effects ($pCO_{2\ heating/cooling}$) (Fig.
589 9). The difference between $pCO_{2\ gas\ exchange}$ and $pCO_{2\ mixing}$ ($\Delta pCO_{2\ gas\ exchange}$) was attributed to gas
590 exchange, whereas the difference between $pCO_{2\ heating/cooling}$ and $pCO_{2\ mixing}$ ($\Delta pCO_{2\ heating/cooling}$) was
591 attributed to thermal effects. Finally, the residual difference between $pCO_{2\ measured}$ and $pCO_{2\ gas\ exchange}$ +
592 $pCO_{2\ heating/cooling}$ ($\Delta pCO_{2\ residual}$) was assigned to ecosystem metabolism (Fig. 9).

593 During low river flow, the values of $\Delta pCO_{2\ gas\ exchange}$ were positive along the entire salinity gradient in
594 all sampling campaigns, with higher values at low salinities (<10), indicating strong CO_2 invasion that
595 increases the values of pCO_2 in the water (Fig. 9d,e). During the rainy period, the low salinities also
596 showed the highest $\Delta pCO_{2\ gas\ exchange}$ deviations, but with negative values, indicating the influence of
597 CO_2 evasion that decreases the values of pCO_2 (Fig. 9f). This shows that the maximal influence of gas
598 exchange on pCO_2 variability during estuarine mixing occurs at low salinities. The influence of gas
599 exchange on pCO_2 showed a marked decrease tendency seaward, with nearly negligible influence
600 from salinities >10, as a result of higher buffering capacity and lower air-water pCO_2 gradient. In
601 addition, in intermediate and high salinity waters, pCO_2 values remain very close to air pCO_2 values,
602 minimizing the effect of atmospheric gas exchange. Consequently, during estuarine mixing in the
603 PSRE, the process of gas exchange has a significant impact on DIC concentrations, particularly in the
604 low-buffered waters of the river domain (Fig. S2; Supplementary information). The highest influence
605 of CO_2 invasion was verified on October 17, when the highest wind and gas transfer velocities were
606 observed (Table 3) and $\Delta pCO_{2\ gas\ exchange}$ reached a value of 50 ppmv (Fig. 9b,e). The highest influence
607 of CO_2 evasion was verified on March 18, when the $\Delta pCO_{2\ gas\ exchange}$ reached a value of -150 ppmv
608 (Fig 9f). For intermediate and high salinity waters, the influence of gas exchange on pCO_2 variability
609 was minor and nearly negligible, close to that of the marine endmember. Indeed, previous studies have
610 reported lower buffering capacities in regions dominated by freshwaters when the freshwater
611 endmember present low TA concentrations (Hu and Cai, 2013; Cai et al., 2013).

612 The values of $\Delta pCO_{2\ cooling/heating}$ were almost always positive, indicating that the water in the estuarine
613 zone was warmed compared to expected behavior for two endmembers mixing. The highest values of
614 $\Delta pCO_{2\ cooling/heating}$ occurred in mid- to high-salinity waters (salinity values of 20-30). These salinities
615 were generally sampled around midday, when solar irradiance is highest, thus causing this thermal
616 effect. For these salinities of the PSRE, the increase of 1 °C in water temperature tend to increase
617 pCO_2 by ~15 ppmv. As the difference between the temperature measured *in situ* and that predicted by
618 the conservative mixing mean of approximately +0.8 °C, the influence of heating was 12 ppmv, on
619 average; however, the heating effect could reach up ~30 ppmv of pCO_2 under conditions of high

intensity solar irradiance during sampling in summer, particularly on the Mar 18 sampling (Fig.9c,f). An exception occurred during sampling on February 17, when water cooling was observed at low salinities (Fig. 9a,d). In addition to local thermal effects occurring at the time scale of estuarine mixing, seasonal variation in temperature induced variations in pCO_2 mainly in waters with salinity >30, resulting in approximately one half (30 ppmv) of the pCO_2 difference between summer and winter (Takahashi et al. 2002). Indeed, pCO_2 variability in the oligotrophic surface waters of the continental shelf of the Southwestern Subtropical Atlantic Ocean is mainly driven by temperature (Ito et al., 2005). The continental shelf of southeastern Brazil, where the river plume of the PSRE is located, is influenced by the Western Boundary Current, which flows southward along the Brazilian shelf as a section of the South Atlantic Ocean subtropical gyre (Campos et al., 2000). The Brazil Current carries the Tropical Water in the upper layers, the South Atlantic Central Water at intermediate depths, in addition to the Coastal Water in the inner portion of continental shelves, which compose the water masses in the region (Castro and Miranda, 1998).

In general, the differences between $pCO_{2\ measured}$ and $pCO_{2\ mixing}$ were positive for all sampling campaigns, with deviation means of +45 ppmv, +30 ppmv and +32 ppmv for the Feb 17, Oct 17 and Feb 18 samplings, respectively (Fig. 9d,e,f). Together, the gas exchange and thermal effects accounted for nearly half of this difference (with gas exchange and water heating corresponding to approximately 18% and 36%, respectively), whereas the other half (residual difference, $\Delta pCO_{2\ residual}$) was attributed to the ecosystem metabolism along the mixing zone. These positive deviations reveal a CO_2 production along the mixing zone that is not linked to conservative mixing, gas exchange and thermal variability, but rather to net heterotrophy during estuarine mixing. However, some negative $\Delta pCO_{2\ residual}$ values were also observed in low salinity waters under low river flow conditions, which shows a net biological CO_2 uptake by phytoplanktonic primary production. At low salinities in summer, some autotrophy decreases $pCO_{2\ measured}$ values in relation to those of $pCO_{2\ mixing}$.

4.3 Impact of phytoplankton on the river and low salinity region

Phytoplankton had an important impact on pCO_2 in the low salinity region of the PSRE, as revealed by the Chl *a* concentrations (Fig. 4j,k,l), the δ^{13}C-DIC signatures (Fig. 4g,h,i), and by the mixing model presented in the previous section (Fig. 9). During low river flow, the PSRE presented an atypical pattern of pCO_2 variability along the salinity gradient. In that period, Chl *a* concentrations were higher in the fresh and low salinity waters, with a strong negative correlation with water pCO_2, showing an uptake by planktonic primary production (Fig. 5). This inverse correlation between Chl *a* and pCO_2 occurred only during low river flow, when the lower hydrological model forcing provides favorable conditions for phytoplankton growth in freshwaters because of the high availability of nutrients, high incidence of photosynthetically active radiance, increased water residence time, and formation of

vertical water column stratification (Souza et al., 2010; Cotovicz et al., 2013). The freshwater discharge contributes to maintaining low dilution and flushing potentials, changing the trophic status in the estuary from oligotrophic to mesotrophic (Cotovicz Jr. et al., 2013). Uptake of CO_2 by phytoplankton is also evidenced by the negative and significant relationship between pCO_2, DO, and δ^{13}C-DIC signatures (Fig. S3, Supplementary information). During low river flow, pCO_2 values were lower, whereas DO concentrations and δ^{13}C-DIC signatures were higher, indicating prevalence of net autotrophy. During photosynthesis, plants preferentially utilize the lighter carbon isotope (^{12}C) rather than the heavier carbon isotope (^{13}C), making the remaining DIC pool ^{13}C enriched (Finlay and Kendall, 2007; Cotovicz et al., 2019). A previous study showed that the stable isotope composition of the dissolved CO^2 (δ^{13}C-DOC) also presented a marked seasonal signal in the PSRE, with more ^{13}C depletion in the rainy season (minimum of -25.7 ‰) than in the dry season (maximum of -20.0 ‰) (Marques et al., 2017). These authors suggested that algae could be a potential source of isotopically heavier DOC to the river zone during the dry season, as our data of low pCO_2 values and high δ^{13}C-DIC signatures and Chl *a* concentrations also suggest.

The Paraiba do Sul River receives large amounts of domestic and industrial effluents along its course, which drains one of the most urbanized and industrialized regions of Brazil (Cotovicz et al., 2013). Low pCO_2 levels due to nutrient enrichment and phytoplankton blooms development has been previously shown for other coastal bays surrounded by large urban areas, e.g., the tropical Guanabara Bay (Cotovicz et al., 2015) and in the temperate Tokyo Bay (Kubo et al., 2017). However, this is very uncommon in river-dominated estuaries, which are considered important CO_2 sources globally (Borges and Abril, 2011). To the best of our knowledge, this pattern of low pCO_2 in freshwater was only reported in the temperate Merrimack Estuary, located in a highly industrialized region of the United States, which experienced a rapid population growth (Salisbury et al., 2008).

Large phytoplankton biomass is observed in the freshwaters of the PSRE during low river flow, but it shows a marked decline seaward (Fig. 4j,k,l). Indeed, estuarine deltas with short residence times are characterized by rapid salinity changes in water masses, which hinder the installation of phytoplankton communities because of osmotic stress (Lancelot and Muymaert, 2011). Salinity and turbulent mixing are often reported as the major factors determining phytoplankton distribution (Cloern, 1996; Lancelot and Muylaert, 2011). In addition to osmotic stress, the community structure, biomass production, species succession, and magnitude of the phytoplankton bloom along the estuary are also related to small availability and short residence time (Roubeix et al., 2008; Flöder et al., 2010). Thus, sharp salinity changes, high turbulence, turbidity, and short residence time create conditions unfavorable for phytoplankton production.

During high river flow, the phytoplankton community is probably flushed and dies in the main channel. The river discharge is stronger than the tidal prism, and the mixing occurs offshore.

According to Lucas et al. (2009), the phytoplankton biomass can increase in an estuary only if the net specific growth rates exceed the water residence time and flushing time in the estuary. In general, development of phytoplankton blooms in estuaries is inversely correlated to river water discharge (Strayer et al., 2008). However, during the flood on May 18, part of the phytoplankton was apparently trapped in the low salinity mangrove creeks, where the observed Chl *a* concentrations reached ~70 µg L^{-1} (Table 2). Mangrove creek provided ideal conditions for phytoplankton refuge due to low salinity stress. This created a special case in this estuary - a low salinity mangrove creek enriched with phytoplankton. Phytoplankton activity and the influence on DIC and δ^{13}C-DIC concentrations are evident in the mangrove creek within the diurnal variations (Fig. 6). During the diel sampling in the mangrove creek, phytoplankton biomass was high, and managed to drawdown pCO_2 during the afternoon compare with nighttime, making δ^{13}C-DIC less negative due to a preferential uptake of ^{12}C from the DIC pool during photosynthesis. Similar processes have been described in a hypertrophic lake (Lake Taihu, China; Van Dam et al., 2018b) and in a tropical eutrophic coastal embayment (Guanabara Bay, Brazil, Cotovicz Jr. et al., 2019), but not in mangrove creeks. During the rainy period, the mangrove creek presented more ^{13}C-enriched signatures than the expected for conservative mixing (Fig. 4g,h,i) and related to this phytoplankton activity. However, this pattern in the mangrove creek was not verified during the dry period, when Chl *a* concentration do not exceed 14.6 µg L^{-1}, and δ^{13}C-DIC signatures were ^{13}C-depleted more than would be expected for conservative mixing, a distribution generally found in mangrove-dominated waters because of enhanced respiratory processes (Bouillon et al., 2007; 2011; Miyajima et al., 2009; Sippo et al., 2016).

4.4. Evidence of heterotrophy in the mixing zone

Multiplication of the residual pCO_2 difference attributed to biological activities ($\Delta pCO_{2\ residual}$) with gas transfer velocity (Eq. 3) provides an estimate of the community production (NCP) (Table 4). The gas transfer velocity parameterization of Raymond and Cole (2001), which resulted in intermediate values of air-water fluxes (Table 3), was chosen for this calculation. For the entire estuarine mixing zone, average NCP was -1.70 mmol m^{-2} d^{-1} on February 17, -1.13 mmol m^{-2} d^{-1} on October 17, and -0.58 mmol m^{-2} d^{-1} on February 18. NCP values in the PSRE are in the lower range of NCP and ecosystem metabolism in the European coastal zone (Gazeau et al., 2004). These low NCP values observed along the mixing zone of the PSRE confirm the moderate influence of biological activities, with microbial respiration not being sufficient to create CO_2 oversaturation in relation to the atmosphere. During low river flow, the entire mixing zone was already undersaturated, and the net heterotrophy was also not sufficient to generate CO_2 outgassing. This created a very special condition in the mixing zone of the estuary, with concomitant pCO_2 undersaturation and heterotrophic metabolism. During high river flow, the heterotrophic metabolism was also apparent in the freshwater owing to pCO_2 values above the atmospheric equilibrium, DO concentrations below the atmospheric equilibrium, and more negative δ^{13}C-DIC signatures, all indicating prevalence of microbial respiration over primary

production (Fig. S3, Supplementary information). However, as previously shown (Fig 9f), heterotrophic metabolism was modest in the estuary during high discharge, and thus the river input was a major contributor to the high CO_2 concentrations, at least in the region dominated by freshwaters (0-5 salinity). Riverine CO_2 inputs represent the major CO_2 source in other river-dominated estuaries (Jiang et al., 2008; Joesoef et al., 2015; Van Dam et al., 2018a).

The covariations of $\Delta\delta^{13}$C-DIC and ΔDIC, considering only the main river channel, also reveal net heterotrophy, with values of δ^{13}C-DIC showing slight ^{13}C-depleted signatures (negative $\Delta\delta^{13}$C-DIC) compared with the conservative mixing (Fig. 10). This graph is divided in four quadrants that represent the processes of primary production/outgassing of CO_2 (quadrant PP/OG), carbonate precipitation (quadrant CP), organic carbon degradation (quadrant DC), and carbonate dissolution (quadrant CD) (Alling et al., 2012; Samanta et al., 2015; Cotovicz et al., 2019). The red arrows represent the directions of slopes in which data points would move in relation to a specific process, whereas the grey lines represent the directions in which samples would move in relation to the effects of more than one process (see figure caption for further details). The data points of the PSRE are mostly located in the quadrant of organic carbon degradation (DC), and to a lesser extent in the quadrant of carbonate precipitation (CP). The process of organic carbon degradation increases the DIC concentrations in water (positive ΔDIC) and decreases the isotopic signature of DIC (negative $\Delta\delta^{13}$C-DIC) (Alling et al., 2012; Samanta et al., 2015). The respiration of organic carbon produces CO_2 with approximately the same isotopic signature than that of the respired organic matter, which is generally ^{13}C depleted; consequently, the DIC pool tends to be more depleted in ^{13}C when the organic matter respiration rates are high and prevalent in phytoplankton uptake (Kendall et al., 2004; Bouillon et al., 2011; Borges et al., 2018). The process of carbonate precipitation is unlikely to occur, because this estuary is not known to host high levels of calcifying fauna and flora. However, as pointed out, DIC and δ^{13}C-DIC can be subjected to more than one process at same time. This means that if one sample was subjected to organic carbon degradation followed by CO_2 outgassing, it could also be located in the quadrant of carbonate precipitation (Samanta et al., 2015). This probably occurs in regions that are sources of CO_2 to the atmosphere: the mixing region with very low salinities on March 18 and in offshore waters on Feb 17 and Mar 18 (Figs. 9 and 10). These deviations of δ^{13}C-DIC signatures and DIC concentrations from the conservative mixing are thus very consistent with the approach, considering the differences between $pCO_{2\ measured}$ and $pCO_{2\ mixing}$ (Fig. 9).

The marked seaward decrease of Chl *a* concentrations along the mixing zone in the main channel suggests that these phytoplankton cells are dying, providing labile organic material for decomposition by heterotrophic bacteria. However, heterotrophy remains weak probably because of the short water residence time in the mixing zone, a crucial factor for bacterial growth in estuaries (Del Giorgio and Bouvier, 2002; Crump et al., 2004), and because of salinity stress in the bacterioplankton, since that freshwater bacteria could remain active in the estuary, but at a reduced rate (Crump et al., 2004). The

762 ΔTA and ΔDIC values along the salinity gradient in the main channel were low (generally <50 µmol
763 kg^{-1}; Fig. 8b), which correspond to less than 5% of the DIC and TA pools, confirming a modest
764 biological influence in the main channel.

765

766 4.5 Tidal pumping in the mangrove creek

767 Water pCO_2 values in the mangrove creek were much higher than those in the main channel, as well as
768 than those predicted by the conservative mixing curve (Fig.3). In addition, the mean pCO_2 values
769 observed in the mangrove creeks were within the high range of values reported in other mangroves
770 worldwide. The maximum pCO_2 value reported here was 22,000 ppmv and, to the best of our
771 knowledge, only one study reported a higher maximum pCO_2 value (27,000 ppmv; Australian micro-
772 tidal system, Call et al. 2015). Our measured pCO_2 values are similar to those observed in some micro-
773 , meso- (Koné and Borges, 2008; Call et al., 2015; Rosentreter et al., 2018) and macro-tidal (Call et
774 al., 2019) mangrove creeks. The mangrove waters presented higher values of ΔTA and ΔDIC
775 compared with those of the main channel (Fig. 8b). The slope of the linear regression of ΔTA *vs*.
776 ΔDIC in the mangrove creek was 0.73, a value within the theoretical slopes of organic matter aerobic
777 degradation (0.2), denitrification (0.8), sulfate reduction (0.9), and calcium carbonate ($CaCO_3$)
778 dissolution (2.0) (Borges et al., 2003; Bouillon et al., 2007). Denitrification is likely to be minor in
779 mangrove ecosystems due to the low concentrations of inorganic N-species (Alongi et al., 2000;
780 Maher et al., 2016). $CaCO_3$ dissolution is unlike to be important in this mangrove that does not receive
781 important amounts of $CaCO_3$ from adjacent ecosystems. This slope is rather similar to those found in
782 the mangrove tidal creeks of Papua New Guinea (Borges et al., 2003), Kenya (Bouillon et al. 2007)
783 and Australia (Sippo et al., 2016) and in the secondary channels of the Mekong Delta (Borges et al.,
784 2018), suggesting that the main processes responsible for TA and DIC production are sulphate
785 reduction and aerobic degradation of organic matter. TA production occurs when DO presents
786 saturation <30% (Fig. 7b), and it is maximal under hypoxic/anoxic conditions. These results reveal
787 that the mangrove creek in the PSRE is producing and exporting DIC and TA to mangrove
788 surrounding waters, a process recently reported in a number of other mangroves that still needs precise
789 quantification (Sippo et al., 2016; and references there in). Important correlations of radon (^{222}Rn) with
790 DIC and TA in several mangrove creeks located at different coastal latitudes have evidenced an
791 important production of TA and DIC in mangrove sediment pore waters with export mediated by
792 tidally induced processes (Santos et al., 2018; Call et al., 2019 and references therein).

793 The relationship between E-DIC and AOU (Fig. 08a) exhibited important deviations above the 1:1 line
794 that occurred almost exclusively in the mangrove creek. This high deviation above the 1:1 line in the
795 mangrove creek could be associated with anaerobic organic matter degradation in sediments and
796 lateral transfer via tidal pumping. Because the process of sulphate reduction is a dominant

mineralization pathway of organic carbon in mangroves (Borges et al., 2003; Bouillon et al., 2007; Sippo et al., 2016), secondary metabolites such as Fe(II) and sulfides escape re-oxidation by oxygen through the formation of pyrite (Alongi et al., 2000; Hu and Cai, 2011), resulting in net consumption of protons and net production of TA.

Tidal variation also seems to be important considering the modulation of CO_2 production and consumption in the mangrove tidal creek (Figs. 6 and 7). On May 2017, CO_2 uptake occurred during daytime, making the waters enriched in δ^{13}C-DIC, with drawdown of pCO_2 and production of DO, even during ebb tide. This explains the low pCO_2 values at ebb tide (daytime), which are not common in mangrove waters (Bouillon et al., 2011; Sippo et al., 2016). The maximal CO_2 concentrations were found during ebb tide in early morning, concomitant with the highest concentrations of TA and DIC and the highest ^{13}C depletion, evidencing the carbon respiration accumulated overnight and the influence of diagenetic processes. Tidal pumping is facilitated, during ebb tide, by the semi-diurnal flushing of crab burrows that are considerably enriched in dissolved carbon due to the diffusion and advection of pore water from the soils (Borges et al., 2003; Call et al., 2015; Maher et al., 2015). This pCO_2 pattern peaking at the nighttime ebb tide is consistent with findings of previous studies that suggest a pore water source of surface water pCO_2 (Bouillon et al., 2007; Kristensen et al., 2008; Linto et al., 2014; Call et al., 2019).

4.6 CO_2 fluxes in the PSRE compared with those of other estuaries

Estuarine systems and mangrove surrounding waters are sources of CO_2 to the atmosphere and significant for regional and global carbon budgets (Bouillon et al., 2008; Maher et al., 2013; Chen et al., 2013; Laruelle et al., 2013). According to the most recent global compilation of estuarine CO_2 emissions propose by Chen et al. (2013), upper estuaries are CO_2 sources of the order of 106 mmol C m^{-2} d^{-1}, mid-estuaries emit 47 mmol C m^{-2} d^{-1} , and lower estuaries with salinities >25 emit 23 mmol C m^{-2} d^{-1}. These values are much higher than those found in the PSRE, which partially acts as a CO_2 sink, with annual CO_2 emission of only 1.63 to 11.98 mmol C m^{-2} d^{-1} (Table 3). The low CO_2 fluxes in the PSRE are consistent with those found in the continental shelf of the subtropical Atlantic Ocean (0.3-9.8 mmol C m^{-2} d^{-1}; Ito et al., 2005). Considering only the dry period, the estuary as a whole was a CO_2 sink, with fluxes ranging from -0.34 to -5.26 mmol C m^2 d^{-1}. These values are close to those reported in the tropical Aby Lagoon (-7.39 mmolC m^{-2} d^{-1}; Koné et al., 2008), subtropical southeast Australian estuaries (-3.28 to -12.05 mmolC m^{-2} d^{-1}; Maher and Eyre, 2012), the tropical eutrophic Guanabara Bay (-26.3 to -50.1 mmolC m^{-2} d^{-1}; Cotovicz et al., 2015), the temperate Tokyo Bay (-8.8 mmolC m^{-2} d^{-1}; Kubo et al., 2017) and the Liminganlahti Bay (-2.46 mmolC m^{-2} d^{-1}; Silvennoinen et al., 2008), in addition to some fjords (Takahashi et al., 2012). All these systems are marine-dominated estuaries, different from the PSRE, which is a river-dominated estuary. To the best of our knowledge,

only the temperate Kennebec River (-1.36 mmol C m^{-2} d^{-1}; Takahashi et al., 2012) and the New River/USA (-0.5 to 5.4 mmolC m^{-2} d^{-1}; Crosswell et al., 2017) are river-dominated estuaries that exhibited CO_2 sink at least in certain periods of the year. Recent findings in the mixing zone of the Amazon River estuary also calculated a net CO_2 sink (maximum of -9.2 mmol C $m^{-2}d^{-1}$), attributed to mixing and biological activity, although the Amazon River and the tropical Atlantic are net sources (Lefèvre et al., 2017). Considering only the rainy period, the PSRE was a CO_2 source of approximately 5.71 to 19.37 mmol C m^{-2} d^{-1}. These CO_2 emissions are much lower than the average global emissions in estuaries (Chen et al., 2013) due to the fact that, even under high river flow conditions, the mixing zone of the PSRE is a permanent CO_2 sink due to the prevalence of thermodynamic processes. However, considering only the river domain during the rainy season, the PSRE presents emission of approximately 60 mmol C m^{-2} d^{-1}, a degassing rate close to those reported in other river-dominated estuaries (Frankignoulle et al., 1998; Chen et al., 2013).

The CO_2 degassing rate in the mangrove tidal creek (average of 135 mmol C m^{-2} d^{-1}) is above global average of CO_2 flux emissions from surrounding mangrove waters (56 mmol C m^{-2} d^{-1}; Rosentreter et al., 2018). Our mean values and ranges of CO_2 degassing are close to those found in mangroves in Vietnam (Kiên Vàng and Tam Giang mangroves, 32 to 155 mmol C m^{-2} d^{-1}; Koné and Borges, 2008), Andaman Islands (Kalighat mangrove, 23 to 173 mmol C m^{-2} d^{-1}; Linto et al., 2014), Australia (Moreton Bay mangrove tidal creek, 202 mmol C m^{-2} d^{-1}; Call et al., 2015), and the Amazon region (62 to 437 mmol C m^{-2} d^{-1}; Call et al., 2019). These high CO_2 emissions in mangrove tidal creeks, in addition to the mangrove production of TA and DIC and transport to surrounding waters, can represent an important fraction of the carbon that is fixed by mangrove vegetation, with high significance in mangrove carbon budgets on a global scale (Bouillon et al., 2008; Maher et al., 2013, Call et al., 2015).

Comparison between the amount of DIC delivered by the river and the CO_2 exchanges at the air-sea interface in the mixing zone shows that the river contributes ~18 to 520 times more inorganic carbon to the adjacent continental shelf compared with the estuarine carbon sink. This means that the air-water exchange of CO_2 is much slower than the acid-base equilibration of DIC during mixing in the estuary, increasing the importance of thermodynamic processes and decreasing the importance of air-water exchanges and biological activities. It is worth highlighting that many of the world's largest river systems are located in tropical regions, which provide ~40% of global freshwater discharge to the oceans (Dai and Thenberth, 2002). Overall, large tropical rivers present low TA concentrations, such as the Amazon, Congo and Orinoco Rivers (Cai et al., 2008; Moore-Maley et al., 2018). Consequently, the CO_2 concentrations at the estuarine mixing zone of large and poorly buffered rivers can be largely overestimated due to this still overlooked process.

5. Conclusions

Overall, the ecosystem showed aquatic sources and sinks of CO_2 considering specific estuarine regions, which were modulated by carbonate thermodynamics, gas exchange, thermal effects, and biological activities. The pCO_2 and carbonate chemistry parameters in the PSRE showed marked spatiotemporal variations governed by processes somewhat different from those reported so far in the literature:

i) In the freshwater domain, biological effects were prevalent. During high river flow, the waters presented higher pCO_2 values and lower DO concentrations and δ^{13}C-DIC signatures, as a result of heterotrophic processes in the river. In contrast, under dry conditions, the waters presented low pCO_2 values and high δ^{13}C-DIC signatures as a result of phytoplankton growth.

ii) In the mixing zone, the thermodynamic processes during estuarine mixing was the most important driver of pCO_2 variations, with measured pCO_2 following a distribution close to the theoretical conservative curve predicted by the mixing of the river and marine endmembers. During the rainy period, the pCO_2 values decreased sharply as a result of rapid absorption by the acid-base buffering capacity of high TA seawaters. During the dry period, the pCO_2 values were below the atmospheric pCO_2 in freshwater and increased in seaward, also consistent with the theoretical thermodynamic mixing.

iii) The δ^{13}C-DIC signatures were slightly below the conservative mixing curve, indicating a heterotrophic metabolism at intermediate to high salinities. The biological activity contributed to approximately half of the deviation of measured pCO_2 from $pCO_{2\ mixing}$. The other half was attributed to gas exchange (~18%) and water heating (~36%) during estuarine mixing.

iv) In the mangrove creek, the waters presented high CO_2 values in all sampling campaigns, with strong oversaturation attributed to production of DIC and TA in the water and pore waters by aerobic and anaerobic processes, and transport by diffusion and convection via tidal pumping. Interesting to point out that, during high river flow, the mangrove-dominated waters presented higher δ^{13}C-DIC signatures than the main estuarine channel, attributed to phytoplankton growth and fractionation of DIC.

Considering the entire area of the PSRE, the estuary was a CO_2 sink at low freshwater discharge (air-water CO_2 fluxes ranging from -0.34 to -5.26 mmol C m^{-2} d^{-1}) and a CO_2 source at high freshwater discharge (5.71-19.37 mmol C m^{-2} d^{-1}). These fluxes are lower and different from those reported in other river-dominated estuaries worldwide, which are normally strong CO_2 sources. The construction of dams in the upper sections of Paraiba do Sul River has decreased its water flow and, associated with increased anthropogenic-derived nutrient inputs to the river, can potentially change the functioning of this ecosystem, from an annual CO_2 source to an annual CO_2 sink. These results also have implications

on global carbon budgets, showing that tropical river-dominated estuaries could absorb CO_2 along the river and mixing domains as a result of the poor buffering capacity during estuarine mixing. Low TA concentrations are a property of many large tropical rivers (Amazon, Congo, Orinoco), suggesting that this process can be important globally and needs further investigation.

Acknowledgments

The authors are grateful for the support from the Laboratory of Environmental Sciences and to the Graduate Program in Ecology and Natural Resources of the State University of Norte Fluminense Darcy Ribeiro. This study was financed in part by the Coordenação de Aperfeiçoamento de Pessoal de Nível Superior -Brazil (CAPES)-Finance Code 001, and by the Carlos Chagas Foundation for Research Support of the State of Rio de Janeiro (FAPERJ; proc. no. E-26/202.785/2016). Luiz C. Cotovicz Jr. is a postdoctoral researcher of the Carlos Chagas Foundation for Research Support of the State of Rio de Janeiro (FAPERJ; proc. no. E-26202.785/2016). Carlos E. Rezende thanks the financial support of CNPq (305217/2017-8) and FAPERJ (E-26/202.916/2017 and 210.883/2016). B.A. Knoppers is a senior scientist of CNPq (proc. no. 301572/2010-0). Luciana O. Vidal is a postdoctoral researcher of the Foundation for the Coordination of Higher Education and Graduate Training (CAPES; proc. no. 88882.314551/2019-01). This research was also conducted with the support of the International Research Project VELITROP (Vulnerability of littoral tropical ecosystems to eutrophication) funded by the French Institute of Environment and Ecology INEE-CNRS.

References

Abril, G., Etcheber, H., Delille, B., Frankignoulle, M., Borges, A.V., 2003. Carbonate dissolution in the turbid and eutrophic Loire estuary. Mar. Ecol-Prog. Ser. 259, 129–138. https://doi.org/10.3354/meps259129.

Abril, G., Borges, A.V., 2004. Carbon dioxide and methane emissions from estuaries, in: Tremblay, A., Varfalvy, L., Roehm, C., Garneau, M. (Eds.), Greenhouse Gases Emissions from Natural Environments and Hydroelectric Reservoirs: Fluxes and Processes. Springer, Berlin, pp. 187–207.

Abril, G., Commarieu, M.-V., Sottolichio, A., Bretel, P., Guérin, F., 2009. Turbidity limits gas exchange in a large macrotidal estuary. Estuar. Coast. Shelf Sci. 83, 342–348. https://doi.org/10.1016/j.ecss.2009.03.006

Abril, G., Martinez, J.-M., Artigas, L.F., Moreira-Turcq, P., Benedetti, M.F., Vidal, L., Meziane, T., Kim, J.-H., Bernardes, M.C., Savoye, N., Deborde, J., Albéric, P., Souza, M.F.L., Souza, E.L., Roland, F., 2014. Amazon River Carbon Dioxide Outgassing fueled by Wetlands. Nature 505, 395–398. https://doi.org/10.1038/nature12797

Alling, V., Porcelli, D., Mörth, C.M., Anderson, L.G., Sanchez-Garcia, L., Gustafsson, Ö., Andersson, P.S., Humborg, C., 2012. Degradation of terrestrial organic carbon, primary production and out-gassing of CO_2 in the Laptev and East Siberian Seas as inferred from ^{13}C values of DIC. Geochim. Cosmochim. Acta 95, 143–159. https://doi.org/10.1016/j.gca.2012.07.028

Alongi, D.M., Tirendi, F., Trott, L.A., Xuan, T.T., 2000. Benthic decomposition rates and pathways in plantations of the mangrove Rhizophora apiculata in the Mekong delta, Vietnam. Mar. Ecol-Prog. Ser. 194, 87-101. https://doi.org/10.3354/meps194087

Amarante, O.A., Silva, F.J., Rios Filho, L.G., 2002. Atlas Eólico, Estado do Rio de Janeiro. Secretaria de Estado da Energia, da Indústria Naval e do Petróleo, Rio de Janeiro. http://www.cresesb.cepel.br/publicacoes/download/atlas_eolico/AtlasEolicoRJ.pdf (accessed 15 April 2019).

Bauer, J.E., Cai, W.-J., Raymond, P., Bianchi, T.S., Hopkinson, C.S., Regnier, P.G., 2013. The changing carbon cycle of the coastal ocean. Nature 504, 61–70. https://doi.org/10.1038/nature12857

Benson, B.B., Krause, D., 1984. The concentration and isotopic fractionation of oxygen dissolved in freshwater and seawater in equilibrium with the atmosphere. Limnol. Oceanogr. 29, 620–632. https://doi.org/10.4319/lo.1984.29.3.0620

Borges, A.V., Djenidi, S., Lacroix, G., Theate, J., Delille, B., Frankignoulle, M., 2003. Atmospheric CO_2 flux from mangrove surrounding waters. *Geophys. Res. Lett*. **30**, 1558. https://doi.org/10.1029/2003GL017143

Borges, A.V., Abril, G., 2011. Carbon dioxide and methane dynamics in estuaries, in: Wolanski, E., McLusky, D. (Eds*.),* Treatise on estuarine and coastal science, vol 5. Academic Press, Amsterdam, pp. 119–161.

Borges, A.V., Abril, G., Bouillon, S., 2018. Carbon dynamics and CO_2 and CH_4 outgassing in the Mekong delta. Biogeosciences 15, 1093-1114. https://doi.org/10.5194/bg-15-1093-2018.

Bouillon, S., Dehairs, F., Schiettecatte, L.-S., Borges, A.V., 2007. Biogeochemistry of the Tana estuary and delta (northern Kenya). Limnol. Oceanogr. 52, 46–59. https://doi.org/10.4319/lo.2007.52.1.0046

Bouillon, S., Borges, A.V., Castañeda-Moya, E., Diele, K., Dittmar, T., Duke, N.C., Kristensen, E., Lee, S.Y., Marchand, C., Middelburg, J.J., Rivera-Monroy, V., Smith, T.J., Twilley, R.R., 2008. Mangrove production and carbon sinks: a revision of global budget estimates. *Glob.* Biogeochem. Cy. 22, GB2013. https://doi.org/10.1029/2007GB003052.

965 Bouillon, S., Connolly, R.M., Gillikin, D.P., 2011. Use of stable isotopes to understand food webs and
966 ecosystem functioning in estuaries, in: Wolanski, E., McLusky, D. (Eds.), Treatise on Estuarine and
967 Coastal Science. Academic Press, Amsterdam, pp. 143–173.

968 Cai, W.-J., Pomeroy, L.R., Moran, M.A., Wang, Y., 1999. Oxygen and carbon dioxide mass balance
969 for the estuarine–intertidal marsh complex of five rivers in the southeastern U.S. Limnol. Oceanogr.
970 44, 639–649. https://doi.org/10.4319/lo.1999.44.3.0639.

971 Cai, W.-J., Guo, X., Chen, C.-T.A., Dai, M., Zhang, L., Zhai, W., Lohrenz, S.E., Yin, K., Harrison,
972 P.J., Wang, Y., 2008. A comparative overview of weathering intensity and HCO3− flux in the world's
973 major rivers with emphasis on the Changjiang, Huanghe, Zhujiang (Pearl) and Mississippi Rivers.
974 Cont. Shelf Res. 28, 1538–1549. https://doi.org/10.1016/j.csr.2007.10.014

975 Cai, W.-J., 2011. Estuarine and coastal ocean carbon paradox: CO_2 sinks or sites of terrestrial carbon
976 incineration? Ann. Rev. Mar. Sci. 3, 123–145. https://doi.org/10.1146/annurev-marine-120709-142723

977 Cai,W.-J., Hu X., Huang, W.-J., Murrell, M.C., Lehrter, J.C., Lohrenz, S.E., Chou, W.-C., Zhai, W.,
978 Hollibaugh, J.T., Wang, Y., 2011. Acidification of subsurface coastal waters enhanced by
979 eutrophication. *Nat. Geosci*. **4**, 766–770. https://doi.org/10.1038/ngeo1297

980 Cai, W. -J., Chen, C.-T.A., Borges A.V., 2013. Carbon dioxide dynamics and fluxes in coastal waters
981 influenced by river plumes, in: Bianchi, T., Allison, M., Cai, W.-J. (Eds.), Biogeochemical Dynamics
982 at Major River-Coastal Interfaces: Linkages with Global Change. Cambridge University Press,
983 Cambridge, pp. 155-173.

984 Call, M., Maher, D.T., Santos, I.R., Ruiz-Halpern, S., Mangion, P., Sanders, C.J., Erler, D.V., Oakes,
985 J.M., Rosentreter, J., Murray, R., Eyre, B.D., 2015. Spatial and temporal variability of carbon dioxide
986 and methane fluxes over semi-diurnal and spring–neap–spring timescales in a mangrove creek.
987 Geochim. Cosmochim. Acta 150, 211–225. https://doi.org/10.1016/j.gca.2014.11.023

988 Call, M., Santos, I.R., Dittmar, T., Rezende, C.E., Asp, N.E., Maher, D.T., 2019. High pore-water
989 derived CO_2 and CH_4 emissions from a macro-tidal mangrove creek in the Amazon region. Geochim.
990 Cosmochim. Acta 247, 106-120. https://doi.org/10.1016/j.gca.2018.12.029

991 Campos, E.J.D., Velhote, D., Silveira, I.C.A., 2000. Shelf break upwelling driven by Brazil current
992 cyclonic meanders. Geophys. Res. Lett. 27, 751–754. https://doi.org/10.1029/1999GL010502

993 Castro, B.M., Miranda, L.B., 1998. Physical oceanography of the western Atlantic continental shelf
994 located between 4°N and 34°S, in: Robinson, A.R., Brink, K.H. (Eds.), The Sea. John Wiley,
995 Hoboken, pp. 209–251.

Chen, C.T.A., Borges, A.V., 2009. Reconciling opposing views on carbon cycling in the coastal ocean: continental shelves as sinks and near-shore ecosystems as sources of atmospheric CO_2. Deep Sea Res. Part 2 Top. Stud. Oceanogr. 56, 578-590. https://doi.org/10.1016/j.dsr2.2009.01.001.

Chen C.-T.A., Huang, T.-H., Chen, Y.-C., Bai, Y., He, X., Kang, Y., 2013. Air–sea exchanges of CO_2 in the world's coastal seas. Biogeosciences 10, 6509–6544. https://doi.org/10.5194/bg-10-6509-2013

Cloern, J.E., 1996. Phytoplankton bloom dynamics in coastal ecosystems: a review with some general lessons from sustained investigation of San Francisco Bay, California. *Rev Geophys*. **2**, 127–168. https://doi.org/10.1029/96RG00986

Cohen, J.E., Small, C., Mellinger, A., Gallup, J., Sachs, J., Vitousek, P.M., Mooney, H.A., 1997. Estimates of coastal populations. Science 278, 1209–1213. https://doi.org/10.1126/science.278.5341.1209c

Cotovicz, Jr., L.C., Brandini, N., Knoppers, B.A., Mizerkowski, B.D., Sterza, J.M., Ovalle, A.R.C., Medeiros, P.R.P., 2013. Assessment of the trophic status of four coastal lagoons and one estuarine delta, eastern Brazil. Environ. Monit. Assess. 185, 3297-3311. https://doi.org/10.1007/s10661-012-2791-x

Cotovicz, Jr., L.C., Knoppers, B.A., Brandini N., Costa Santos, S.J., Abril, G., 2015. A strong CO_2 sink enhanced by eutrophication in a tropical coastal embayment (Guanabara Bay, Rio de Janeiro, Brazil). Biogeosciences 12, 6125–6146. https://doi.org/10.5194/bg-12-6125-2015

Cotovicz, Jr., L.C., Libardoni, B., Brandini, N., Knoppers, B., Abril, G., 2016. Comparações entre medições em tempo real da pCO_2 aquática com estimativas indiretas em dois estuários tropicais contrastantes: o estuário eutrofizado da Baia de Guanabara (RJ) e o estuário oligotrofico do Rio São Francisco (AL). Quím. Nova 39, 1206–1214. http://dx.doi.org/10.21577/0100-4042.20160145

Cotovicz, Jr., L.C., Knoppers, B.A., Deirmendjian, L., Abril, G., 2019. Sources and sinks of dissolved inorganic carbon in an urban tropical coastal bay revealed by δ^{13}C-DIC signals. Estuar. Coast. Shelf Sci. 220, 185-195. https://doi.org/10.1016/j.ecss.2019.02.048

Crosswell, J.R., Anderson, I.C., Stanhope, J.W., Van Dam, B., Brush, M.J., Ensign, S., Piehler, M.F., McKee, B., Bost, M., Paerl, H.W., 2017. Carbon budget of a shallow, lagoonal estuary: Transformations and source-sink dynamics along the river-estuary-ocean continuum. Limnol. Oceanogr. 62, S29–S45. http://doi.org/10.1002/lno.10631

Crump, B.C., Hopkinson, C. S., Sogin, M. L., Hobbie, J.E., 2004. Microbial biogeography along an estuarine salinity gradient: combined influences of bacterial growth and residence time. *Appl. Environ. Microbiol.* **70**, 1494-1505.2 https://doi.org/10.1128/aem.70.3.1494-1505.2004

1028 Dai, A., Trenberth, K.E., 2002. Estimates of Freshwater Discharge from Continents: Latitudinal and
1029 Seasonal Variations . J. Hydrometeorol. 3, 660-687. https://doi.org/10.1175/1525-
1030 7541(2002)003<0660:EOFDFC>2.0.CO;2

1031 Dai, M., Lu, Z., Zhai, W., Chen, B., Cao, Z., Zhou, K., Cai, W.-J., Chen, C.A., 2009. Diurnal
1032 variations of surface seawater pCO_2 in contrasting coastal environments. Limnol. Oceanogr. 54, 735–
1033 745. https://doi.org/10.4319/lo.2009.54.3.0735.

1034 Del Giorgio, P.A., Bouvier, T., 2002. Linking the physiologic and phylogenetic successions in free-
1035 living bacterial communities along an estuarine salinity gradient. Limnol. Oceanogr. 47, 471-486.
1036 https://doi.org/10.4319/lo.2002.47.2.0471

1037 Deirmendjian, L., Abril, G., 2018. Carbon dioxide degassing at the groundwater-stream-atmosphere
1038 interface: isotopic equilibration and hydrological mass balance in a sandy watershed. *J. Hydrol*. **558**,
1039 129–143. https://doi.org/10.1016/j.jhydrol.2018.01.003

1040 Dickson, A.G., 1990. Thermodynamics of the dissociation of boric acid in synthetic seawater from
1041 273.15 to 318.15 K. Deep-Sea Res. I Oceanogr. Res. Pap. 37, 755–766. https://doi.org/10.1016/0198-
1042 0149(90)90004-F

1043 Dickson, A.G., Millero, F.J., 1987. A comparison of the equilibrium constants for the dissociation of
1044 carbonic acid in seawater media. Deep-Sea Res. 34, 1733–1743. https://doi.org/10.1016/0198-
1045 0149(87)90021-5

1046 Dinauer, A., Mucci, A., 2017. Spatial variability in surface-water pCO_2 and gas exchange in the
1047 world's largest semi-enclosed estuarine system: St. Lawrence Estuary (Canada). Biogeosciences 14,
1048 3221-3237. https://doi.org/10.5194/bg-14-3221-2017

1049 Egleston, E.S., Sabine, C.L., Morel1, F.M., 2010. Revelle revisited: Buffer factors that quantify the
1050 response of ocean chemistry to changes in DIC and alkalinity. Glob. Biogeochem. Cy. 24, GB1002.
1051 http://dpo.org/10.1029/2008GB003407, 2010

1052 Finlay, J.C., Kendall, C., 2007. Stable isotope tracing of temporal and spatial variability in organic
1053 matter sources to freshwater ecosystems, in: Michener, R., Lajtha, K. (Eds.), Stable Isotopes in
1054 Ecology and Environmental Science. Blackwell Publishing, Hong Kong, pp. 283-333.

1055 Flöder, S., Jaschinski, S., Wells, G., Burns, C.W., 2010. Dominance and compensatory growth in
1056 phytoplankton communities under salinity stress. J. Exp. Mar. Bio. Ecol. 395, 223–231.
1057 https://doi.org/10.1016/j.jembe.2010.09.006

1058 Frankignoulle, M., Abril, G., Borges, A., Bourge, I., Canon, C., Delille, B., Libert, E., Theate, J.M.,
1059 1998. Carbon Dioxide Emission from European Estuaries. Science 282, 434–436.
1060 https://doi.org/10.1126/science.282.5388.434

Frankignoulle, M., Borges, A., Biondo, R., 2001. A new design of equilibrator to monitor carbon dioxide in highly dynamic and turbid environments. Water Res. 35, 1344–1347. https://doi.org/10.1016/S0043-1354(00)00369-9

Gattuso, J.-P., Magnan, A., Billé, R., Cheung, W.W.L., Howes, E.L., Joos, F., Allemand, D., Bopp, L., Cooley, S.R., Eakin, C.M., Hoegh-Guldberg, O., Kelly, R.P., Pörtner, H.-O., Rogers, A.D., Baxter, J.M., Laffoley, D., Osborn, D., Rankovic, A., Rochette, J., Sumaila, U.R., Treyer, S., Turley, C., 2015. Contrasting futures for ocean and society from different anthropogenic CO_2 emissions scenarios. Science 349, aac4722. https://doi.org/10.1126/science.aac4722

Gazeau ,F., Smith, S.V, Gentili, B., Frankignoulle, M., Gattuso, J.-P., 2004. The European coastal zone: characterization and first assessment of ecosystem metabolism. Estuar. Coast. Shelf Sci. 60, 673–694. https://doi.org/10.1016/j.ecss.2004.03.007

Gran, G., 1952. Determination of the equivalence point in potentiometric titrations-Part II. *Analyst* **77**, 661–671.

Guérin, F., Abril, G., Serç,a D., Delon, C., Richard, S., Delmas, R., Tremblay, A., Varfalvy, L. 2007. Gas transfer velocities of CO_2 and CH_4 in a tropical reservoir and its river downstream. J. Mar. Syst. 66, 161–172. https://doi.org/10.1016/j.jmarsys.2006.03.019.

Hu, X., Cai, W.-J., 2011. An assessment of ocean margin anaerobic processes on oceanic alkalinity budget. Global Biogeochem. Cy. 25, GB3003. https://doi.org/10.1029/2010GB003859

Hu, X., Cai, W.-J., 2013. Estuarine acidification and minimum buffer zone—A conceptual study. Geophys. Res. Lett. 40, 5176-5181. https://doi.org/10.1002/grl.51000

IBGE., 2018. Instituto Brasileiro de Geografia e Estatistica. https://cidades.ibge.gov.br/brasil/rj/panorama/ (Accessed December 13, 2018).

IPCC., 2013. Climate Change 2013: The Physical Science Basis, in: Stocker et al. (Eds.), Contribution of Working Group I to the Fifth Assessment Report of the Intergovernmental Panel on Climate Change. Cambridge Univ. Press., Cambridge. https://doi.org/doi:10.1017/CBO9781107415324

Ito, R.G., Scheider, B., Thomas, H., 2005. Distribution of surface fCO_2 and air–sea fluxes in the Southwestern subtropical Atlantic and adjacent continental shelf. J. Mar. Syst. 56, 227-242. https://doi.org/10.1016/j.jmarsys.2005.02.005

Jähne, B., Munnich, K.O., Bosinger, R., Dutzi, A., Huber, W., Libner, P., 1987. On parameters influencing air-water exchange. J. Geophys. Res. 92, 1937–1949. https://doi.org/10.1029/JC092iC02p01937

Jiang, L.-Q., Cai ,W.-J., Wang, Y., 2008. A comparative study of carbon dioxide degassing in river- and marine-dominated estuaries. Limnol. Oceanogr. 53, 2603–2615. https://doi.org/10.4319/lo.2008.53.6.2603

Joesoef, A., Huang, W.-J., Gao, Y., Cai, W.-J., 2015. Air–water fluxes and sources of carbon dioxide in the Delaware Estuary: spatial and seasonal variability. Biogeosciences 12, 6085–6101. https://doi.org/10.5194/bg-12-6085-2015

Joos, F., Spahni, R., 2008. Rates of change in natural and anthropogenic radiative forcing over the past 20,000 years. Proc. Natl. Acad. Sci. 105, 1425–1430. https://doi.org/10.1073/pnas.0707386105

Kendall, C., Doctor, D.H., Holland, H.D., Turekian, K.K., 2004. Stable isotope applications in hydrologic studies. Surf. Gr. Water, Weather. Soils 5, 319–364. https://doi.org/10.1016/B0-08-043751-6/05081-7

Knoppers, B.A., Ekau, W., Figueiredo, A.G., 1999. The coast and shelf of East and Northeast Brazil and material transport. Geo-Marine Letters, 19, 171-178. https://doi.org/10.1007/s003670050106

Koné, Y.J.M., Abril, G., Kouadio, K.N., Delille, B., Borges, A.V., 2008. Seasonal Variability of Carbon Dioxide in the Rivers and Lagoons of Ivory Coast (West Africa). Estuar. Coast. 32, 246–260. https://doi.org/10.1007/s12237-008-9121-0

Koné, Y.J.M., Borges, A.V., 2008. Dissolved inorganic carbon dynamics in the waters surrounding forested mangroves of the Ca Mau Province (Vietnam). Estuar. Coast. Shelf Sci. 77, 409–421. https://doi.org/10.1016/j.ecss.2007.10.001

Körtzinger, A., 2003. A significant sink of CO_2 in the tropical Atlantic Ocean associated with the Amazon River plume. Geophys. Res. Lett. 30, 2287. https://doi.org/10.1029/2003GL018841

Kristensen, E., Flindt, M.R., Ulomi, S., Borges, AV., Abril, G., Bouillon, S., 2008. Emission of CO_2 and CH_4 to the atmosphere by sediments and open waters in two Tanzanian mangrove forests. Mar. Ecol. Prog. Ser. 370, 53-67. https://doi.org/10.3354/meps07642

Kubo, A., Maeda, Y., Kanda, J., 2017. A significant net sink for CO_2 in Tokyo Bay. Sci. Rep. 7, 44355. https://doi.org/10.1038/srep44355

Lancelot, C., Muylaert, K., 2011. Trends in Estuarine Phytoplankton Ecology., in: McLusky, D.S., Wolanski, E., (Eds.), Treatise on estuarine and coastal science. Academic Press, Amsterdam, pp. 5-15.

Laruelle, G.G., Dürr, H.H., Lauerwald, R., Hartmann, J., Slomp, C.P., Goossens, N., Regnier, P., 2013. Global multi-scale segmentation of continental and coastal waters from the watersheds to the continental margins. Hydrol. Earth Syst. Sci. 17, 2029–2051. https://doi.org/10.5194/hess-17-2029-2013

Le Quéré, C., Andrew, R.M., Friedlingstein, P., Sitch, S., Hauck, J., Pongratz, J., Pickers, P.A., Korsbakken, J.I., Peters, G.P., Canadell, J.G., Arneth A., Arora, V.K., Barbero, L., Bastos, A., Bopp, L., Chevallier, F., Chini, L.P., Ciais, P., Doney, S.C., Gkritzalis, T., Goll, D.S., Harris, I., Haverd, V., Hoffman, F.M., Hoppema, M., Houghton, R.A., Hurtt, G., Ilyina, T., Jain, A.K., Johannessen, T., Jones, C.D., Kato, E., Keeling, R.F., Goldewijk, K.K., Landschützer, P., Lefèvre, N., Lienert, S., Liu, Z., Lombardozzi, D., Metzl, N., Munro, D.R., Nabel, J.E.M.S., Nakaoka, S.-I., Neill, C., Olsen, A., Ono, T., Patra, P., Peregon, A., Peters, W., Peylin, P., Pfeil, B., Pierrot, D., Poulter, B., Rehder, G., Resplandy, L., Robertson, E., Rocher, M., Rödenbeck, C., Schuster, U., Schwinger, J., Séférian, R., Skjelvan, I., Steinhoff, T., Sutton, A., Tans, P.P., Tian, H., Tilbrook, B., Tubiello, F.N., van der Laan-Luijkx, I.T., van der Werf, G.R., Viovy, N., Walker, A.P., Wiltshire, A.J., Wright, R., Zaehle, S., Zheng, B., 2018. Global Carbon Budget 2018, Earth Syst. Sci. Data 10, 2141-2194. https://doi.org/10.5194/essd-10-2141-2018

Lee, K., Kim, T.W., Byrne, R.H., Millero, F.J., Feely, R.A., Liu, Y.M., 2010. The universal ratio of boron to chlorinity for the North Pacific and North Atlantic oceans. Geochim. Cosmochim. Acta 74, 1801–1811. https://doi.org/10.1016/j.gca.2009.12.027

Lefèvre, N., Montes, M.F., Gaspar, F.L., Rocha, C., Jiang, S., Araujo, M., Ibanhez, S., 2017. Net heterotrophy in the Amazon Continental Shelf changes rapidly to a sink of CO_2 in the outer Amazon Plume. *Front. Mar. Sci*. **4**, 1-16. https://doi.org/10.3389/fmars.2017.00278

Linto, N., Barnes, J., Ramachandran, R., Divia, J., Ramachandran, P., Upstill-Goddard, R.C., 2014. Carbon Dioxide and Methane Emissions from Mangrove-Associated Waters of the Andaman Islands, Bay of Bengal. Estuar. Coast. 37, 381–398. https://doi.org/10.1007/s12237-013-9674-4

Lucas, L.V., Thompson, J.K., Brown, L.R., 2009. Why are diverse relationships observed between phytoplankton biomass and transport time? *Limnol. Oceanogr.* **54**, 381–390. https://doi.org/10.4319/lo.2009.54.1.0381

Ludwig, W., Amiotte-Suchet, P., Munhoven, G., Probst, J.-L., 1998. Atmospheric CO_2 consumption by continental erosion: Present-day controls and implications for the last glacial maximum Global Planet. Change, 17, 107– 120. https://doi.org/10.1016/S0921-8181(98)00016-2.

Maher, D.T., Eyre, B.D., 2012. Carbon budgets for three autotrophic Australian estuaries: Implications for global estimates of the coastal air-water CO_2 flux. Global Biogeochem. Cy. 26, GB1032. https://doi.org/10.1029/2011GB004075

Maher, D.T., Santos, I.R., Golsby-Smith, L., Gleeson, J., Eyre, B.D., 2013. Groundwater-derived dissolved inorganic and organic carbon exports from a mangrove tidal creek: The missing mangrove carbon sink? Limnol. Oceanogr. 58, 475–488. https://doi.org/doi:10.4319/lo.2013.58.2.0475

1157 Maher, D.T., Cowley, K., Santos, I.R., Macklin, P., Eyre, B.D., 2015. Methane and carbon dioxide
1158 dynamics in a subtropical estuary over a diel cycle: Insights from automated in situ radioactive and
1159 stable isotope measurements. Mar. Chem. 168, 69–79. https://doi.org/10.1016/j.marchem.2014.10.017

1160 Maher, D.T., Sippo, J., Tait, D., Holloway, C., Santos, I.R., 2016. Pristine mangrove creek waters are
1161 a sink of nitrous oxide. Scientific Reports, 6, 25701. https://doi.org/10.1038/srep25701

1162 Marques, J.S.J., Dittmar, T., Niggemann, J., Almeida, M.G., Gomez-Saez, G.V., Rezende, C.E., 2017.
1163 Dissolved Black Carbon in the Headwaters-to-Ocean Continuum of Paraíba Do Sul River, Brazil.
1164 Front. Earth Sci. 5, 1–12. https://doi.org/10.3389/feart.2017.00011

1165 Mehrbach, C., Cuberson, C.H., Hawley, J.E., Pytkowicz, R.M., 1973. Measurements of the apparent
1166 dissociation constants of carbonic acid in seawater at atmospheric pressure. Limnol. Oceanogr. 18,
1167 897–907. https://doi.org/10.4319/lo.1973.18.6.0897

1168 Miyajima, T., Miyajima, Y., Hanba, Y.T., Yoshii, K., Koitabashi, T., Wada, E., 1995. Determining the
1169 stable isotope ratio of total dissolved inorganic carbon in lake water by GC/C/IIRMS. Limnol.
1170 Oceanog. 40, 994–1000. https://doi.org/10.4319/lo.1995.40.5.0994.

1171 Miyajima, T., Tsuboi, Y., Tanaka, Y., Koike, I., 2009. Export of inorganic carbon from two Southeast
1172 Asian mangrove forests to adjacent estuaries as estimated by the stable isotope composition of
1173 dissolved inorganic carbon. J. Geophys. Res. Biogeosciences 114, 1–12.
1174 https://doi.org/10.1029/2008JG000861

1175 Mook, W.G., Koene, B.K., 1975. Chemistry of dissolved inorganic carbon in estuarine and coastal
1176 brackish waters. Estuar. Coast. Mar. Sci. 3, 325-336.

1177 Mook, W.G., Tan, F.C., 1991. Stable carbon isotopes in rivers and estuaries, in: Degens, E.T., Kempe,
1178 S., Richey, J.E., (Eds.), Biogeochemistry of Major World Rivers. John Wiley and Sons, Chichester,
1179 pp. 245–264.

1180 Moore-Maley, B., Ianson, D., Allen, S.E., 2018. The sensitivity of estuarine aragonite saturation state
1181 and pH to the carbonate chemistry of a freshet-dominated river. Biogeosciences 15, 3743-3760.
1182 https://doi.org/10.5194/bg-15-3743-2018

1183 NOAA, 2019. National Oceanic and Atmospheric Administration. Earth System Research Laboratory.
1184 Global Monitoring Division. https://www.esrl.noaa.gov/gmd/ccgg/trends/graph.html (Accessed 24
1185 July 2019).

1186 Orr, J.C., Epitalon, J.-M., Dickson, A.G., Gattuso, J.-P., 2018. Routine uncertainty propagation for the
1187 marine carbon dioxide system. Mar. Chem. 207, 84–107.
1188 https://doi.org/10.1016/j.marchem.2018.10.006

Ovalle, A.R.C., Silva, C.F., Rezende, C.E., Gatts, C.E.N., Suzuki, M.S., Figueiredo, R.O., 2013. Long-term trends in hydrochemistry in the Paraíba do Sul River, southeastern Brazil. J. Hydrol. 481, 191–203. https://doi.org/10.1016/j.jhydrol.2012.12.036

Raymond, P.A., Cole, J.J., 2001. Gas Exchange in Rivers and Estuaries: Choosing a Gas Transfer Velocity. Estuaries 24, 312-317. https://doi.org/10.2307/1352954

Revelle, R., Suess, H.E., 1957. Carbon dioxide exchange between atmosphere and ocean and the question of an increase of atmospheric CO2 during the past decades. Tellus, 9, 18– 27.

Robbins, L.L., Hansen, M.E., Kleypas, J.A., Meylan,S.C., 2010.CO_2 Calc: a user-friendly seawater carbon calculator for Windows, Max OS X, and iOS (iPhone), U.S. Geological Survey Open-File Report, 2010–1280, 1–17. http://pubs.usgs.gov/of/2010/1280/ (accessed 07 November 2018).

Rosentreter, J.A., Maher, D.T., Erler, D.V., Murray, R., Eyre, B.D., 2018. Seasonal and temporal CO_2 dynamics in three tropical mangrove creeks – A revision of global mangrove CO_2 emissions. Geochim. Cosmochim. Acta 222, 729–745. https://doi.org/10.1016/j.gca.2017.11.026

Roubeix V., Rousseau V., Lancelot C. (2008) Diatom succession and silicon removal from freshwater in estuarine mixing zones: from experiment to modelling. *Estuar. Coast. Shelf Sci*. **78**, 14–26

Rudorff, N.M., Kampel, M., Rezende, C.E., 2011. Spectral mapping of the Paraıba do Sul River plume (Brazil) using multitemporal Landsat images. J. App. Rem. Sens. 5, 053550-053550-19. https://doi.org/10.1117/1.3630220

Salisbury, J.E., 2008. Coastal Acidification by Rivers: A Threat to Shellfish? Eos 89, 513-528. https://doi.org/10.1029/2008EO500001

Salisbury, J.E., Vandemark, D., Hunt, C.W., Campbell, J.W., McGillis, W.R., McDowell, W.H., 2008. Seasonal observations of surface waters in two Gulf of Maine estuary-plume systems: Relationships between watershed attributes, optical measurements and surface pCO_2. Estuar. Coast. Shelf Sci. 77, 245–252. https://doi.org/10.1016/j.ecss.2007.09.033

Samanta, S., Dalai, T.K., Pattanaik, J.K., Rai, S.K., Mazumdar, A., 2015. Dissolved inorganic carbon (DIC) and its ^{13}C in the Ganga (Hooghly) River estuary, India: Evidence of DIC generation via organic carbon degradation and carbonate dissolution. Geochim. Cosmochim. Acta 165, 226–248. https://doi.org/10.1016/j.gca.2015.05.040

Santos, I.R., Maher, D.T., Eyre, B.D., 2012. Coupling automated radon and carbon dioxide measurements in coastal waters. Environ. Sci. Technol. 46, 7685–91. https://doi.org/10.1021/es301961b

Santos, I.R., Maher, D.T., Larkin, R., Webb, J., Sanders, C.J., 2018. Carbon outwelling and outgassing vs. burial in an estuarine tidal creek surrounded by mangrove and saltmarsh wetlands. Limnol. Oceangr. 64, 996-1013. https://doi.org/10.1002/lno.11090

Silvennoinen, H., Liikanen, A., Rintala, J., Martikainen, P.J., 2008. Greenhouse gas fluxes from the eutrophic Temmesjoki River and its Estuary in the Liminganlahti Bay (the Baltic Sea). Biogeochemistry 90, 193–208. https://doi.org/10.1007/s10533-008-9244-1

Sippo, J.Z., Maher, D.T., Tait, D.R., Holloway, C., Santos, I.R., 2016. Are mangroves drivers or buffers of coastal acidification? Insights from alkalinity and dissolved inorganic carbon export estimates across a latitudinal transect. Global Biogeochem. Cy. 30, 753–766. https://doi.org/10.1002/2015GB005324

Souza, T.A., Godoy, J.M., Godoy, M.L.D.P., Moreira, I., Carvalho, Z.L., Salomão, M.S.M.B., Rezende, C.E., 2010. Use of multitracers for the study of water mixing in the Paraíba do Sul River estuary. J. Environ. Radioact. 101, 564–570. https://doi.org/10.1016/j.jenvrad.2009.11.001

Sterza, J.M., Fernandes, L.L., 2006. Distribution and abundance of cladocera (brachiopoda) in the Paraiba do Sul River Estuary, Rio de Janeiro, Brazil. Braz. J. Oceanogr. 54, 193-204. http://dx.doi.org/10.1590/S1679-87592006000300003

Strayer, D.L., Pace, M.L. Caraco, N.F., Cole, J.J., Findlay, S., 2008. Hydrology and grazing jointly control a large-river food web. *Ecology* **89**, 12–18. https://doi.org/10.1890/07-0979.1

Strickland, J.D.H., Parsons, T.R., 1972. A practical handbook of seawater analysis. Fisheries Research Board of Canada Bulletin, Ottawa.

Takahashi, T., Sutherland, S.C., Sweeney, C., Poisson, A., Metzl, N., Tilbrook, B., Bates, N., Wanninkhof, R., Feely, R.A., Sabine, C., Olafsson, J., Nojiri, Y., 2002. Global sea-air CO_2 flux based on climatological surface ocean pCO_2, and seasonal biological and temperature effects. Deep. Sea Res. Part II 49, 1601–1622. https://doi.org/10.1016/S0967-0645(02)00003-6).

Takahashi, T., Sutherland, S.C., Kozyr, A., 2012. Global ocean surface water partial pressure of CO_2 database: Measurements performed during 1957–2011 (Version 2011), Oak Ridge, Tennessee. https://doi.org/10.3334/CDIAC/OTG.NDP088(V2013)

Ternon, J.F., Oudot, C., Dessier, A., Diverrès, D., 2000. A seasonal tropical sink for atmospheric CO_2 in the Atlantic ocean: the role of the Amazon River discharge. Mar. Chem. 68, 183–201. https://doi.org/10.1016/S0304-4203(99)00077-8

Van Dam, B. R., Crosswell, J. R., Anderson, I. C., Paerl, H. W., 2018a. Watershed-scale drivers of air-water CO_2 exchanges in two lagoonal North Carolina (USA) estuaries. J. Geophys. Res. Biogeosciences, 123, 1-17. https://doi.org/10.1002/2017JG004243

Van Dam, B.R., Tobias, C., Holbach, A., Paerl, H.W., Zhu, G., 2018b. CO_2 limited conditions favor cyanobacteria in a hypereutrophic lake: An empirical and theoretical stable isotope study. Limnol. Oceanogr. 63, 1643–1659. https://doi.org/10.1002/lno.10798

Wanninkhof, R., 1992. Relationship Between Wind Speed and Gas Exchange. J. Geophys. Res. 97, 7373–7382. https://doi.org/10.1029/92JC00188

Wanninkhof ,R., 2014. Relationship between wind speed and gas exchange over the ocean revisited. Limnol. Oceanogr. Methods 12, 351–362. https://doi.org/10.4319/lom.2014.12.351

Weiss, R.F., 1974. Carbon dioxide in water and seawater: the solubility of a non-ideal gas. Mar. Chem. 2, 203–215. https://doi.org/10.1016/0304-4203(74)90015-2

Whitfield, M., Turner, D.R., 1986. The carbon dioxide system in estuaries – An inorganic perspective. Sci. Total Environ. 49, 235-255. https://doi.org/10.1016/0048-9697(86)90243-3

Willeit, M., Ganopolski, A., Calov, R., Brovkin, V., 2019. Mid-Pleistocene transition in glacial cycles explained by declining CO2 and regolith removal. Sci. Adv. 5, 1–9. doi:10.1126/sciadv.aav7337

Zhai, W., Dai, M., Guo, X., 2007. Carbonate system and CO2 degassing fluxes in the inner estuary of Changjiang (Yangtze) River, China. Mar. Chem. 107, 342–356. https://doi.org/10.1016/j.marchem.2007.02.011

Table 1 Mean (±standard deviation), minimum and maximum values of the principal physicochemical properties on the waters of the PSRE, separated by sampling campaigns and estuarine zones.

Salinity Interval / Estuarine Region	Sal.	Temp. (°C)	pCO_2 (ppmv)	DIC (µmol kg-1)	pH (NBS)	TA (µmol kg-1)	δ^{13}C-DIC (‰)	Chl *a* (µg L-1)	DO (%sat)
Feb. – 17									
0 – 5	0.8 ± 1.0	30.8 ± 0.4	157 ± 47	428 ± 72	8.40 ± 0.36	441 ± 91	-3.64 ± 0.56	15.3 ± 4.7	110 ± 6
	(0.0 / 4.9)	(28.1 / 31.8)	(41 / 321)	(357 / 655)	(7.29 / 9.36)	(347 / 670)	(-4.81 / -2.30)	(8.0 / 21.3)	(91 / 122)
5 – 30	19.0 ± 6.9	29.1 ± 0.5	306 ± 83	1982 ± 79	8.12 0.08	1234 ± 362	0.27 ± 1.07	7.0 ± 1.4	92 ± 4
	(5.3 / 29.8)	(27.3 / 30.7)	(121 / 446)	(1902 / 2061)	(7.61 / 8.61)	(747 / 1882)	(-2.12 / 1.93)	(4.3 / 9.2)	(86 / 102)
> 30	31.8 ± 1.6	27.9 ± 1.0	459 ± 8	1884 ± 130	8.04 ± 0.01	2239 ± 96	2.46 ± 0.11	1.14 ± 0.88	88.4 ± 0.9
	(30.3 / 33.5)	(26.2 / 28.2)	(402 / 472)	(1689 / 2061)	(8.00 / 8.06)	(2143 / 2336)	(2.34± 2.57)	(0.26 /2.02)	(84.1 / 89.5)
Mangrove	1.2 ± 0.3	30.7 ± 0.2	1479 ± 606	784 ± 137	7.49 ± 0.11	719 ± 120	-7.47 ± 0.64	12.8 ± 1.1	99.1 ± 0.7
Creek	(0.5 / 1.7)	(30.3 / 31.3)	(456 / 2840	(647 / 922)	(7.29 / 7.88)	(599 / 839)	(-8.11 / -6.82)	(10.5 / 14.6)	(98.4 / 100.1)
Oct. – 17									
0 – 5	1.1 ± 1.2	25.4 ± 0.3	192 ± 52	440 ± 81	8.40 ± 0.15	458 ± 86	-3.47 ± 0.36	6.04 ± 1.38	107 ± 9
	(0.0 / 4.9)	(24.6 / 26.2)	(91 / 300)	(347 / 558)	(8.06 / 8.77)	(352 / 573)	(-4.23 / -2.89)	(3.86 / 11.86)	(82 / 119)
5 – 30	19.4 ± 6.0	25.6 ± 0.3	275 ± 62	1158 ± 228	8.47 ± 0.05	1306 ± 266	0.46 ± 0.80	2.49 ± 0.31	89 ± 7
	(5.1 / 29.9)	(24.4 / 26.2)	(102 / 414)	(713 / 1629)	(8.05 / 8.66)	(777 / 1874)	(-1.51 / 1.71)	(1.54 / 3.14)	(79 / 116)
> 30	32.0 ± 0.9	24.0 ± 0.5	390 ± 14	1895 ± 38	8.40 ± 0.01	2211 ± 47	2.19 ± 0.23	1.64 ± 1.30	92 ± 5
	(30.1 / 33.0)	(23.4 / 25.0)	(356 / 429)	(1818 / 1941)	(8.37 / 8.44)	(2120 / 2274)	(1.91 / 2.50)	(0.31 / 4.24)	(86 / 111)
Mangrove	5.1 ± 1.1	24.5 ± 0.1	4016 ± 2643	1755 ± 1172	7.44 ± 0.15	1019 ± 211	-8.96 ± 1.53	6.05 ± 1.63	80 ± 14
Creek	(0.1 / 7.2)	(24.0 / 25.2)	(525 / 11514)	(753 / 4687)	(7.13 7.98)	(700 / 1467)	(-11.82 -7.00)	(3.83 / 9.65)	(48 / 112)
Mar. – 18									
0 – 5	0.1 ± 0.13	29.0 ± 0.4	1946 ± 252	469 ± 86	7.10 ± 0.13	428 ± 101	-7.38 ± 1.49	1.81 ± 0.37	58 ± 3
	(0.0 / 4.4)	(28.1 / 31.1)	(1187 / 2411)	(381 / 667)	(6.43 / 8.20)	(337 / 663)	(-9.07 / -4.64)	(0.85 / 2.72)	(58 / 80)
5 – 30	17.4 ± 6.6	29.5 ± 0.8	380 ± 96	1198 215	8.21 ± 0.14	1322 ± 266	0.22 ± 0.86	4.03 ± 1.60	87 ± 6
	(5.1 / 30)	(27.3 / 31.8)	(309 / 668)	(747 / 1628)	(7.79 / 8.42)	(766 / 1846)	(-2.87 / 1.56)	(0.53 / 7.57)	(73 / 107)
> 30	33.7 ± 2.2	28.4 ± 0.5	439 ± 17	1895 ± 129	8.27 ± 0.01	2170 ± 160	2.08 ± 0.25	1.74 ± 1.09	88 ± 3
	(30.1 / 36.2)	(27.5 / 29.3)	(384 / 469)	(1765 / 2024)	(8.24 / 8.32)	(2010 / 2331)	(1.83 / 2.34)	(0.65 / 2.83)	(84 / 94)
Mangrove	0.6 ± 0.3	28.7 ± 0.2	8988 ± 2325	1555 ± 195	6.92 ± 0.09	1177 ± 356	-6.43 ± 1.79	22.70 ± 2.51	29 ± 16
Creek	(0.1 / 2.1)	(28.3 / 30.1)	(3931 / 13344)	(1071 / 2407)	(6.75 / 7.78)	(822 / 2055)	(-9.04 / -3.27)	(19.31 / 26.55)	(3 / 70)

Table 2 Results of the anchored station at the mangrove creek showing the diurnal variability (mean, standard deviation, minimum and maximum) for the principal physicochemical properties k, separated by time of sampling (ebb tide daytime, flood tide nighttime, ebb tide nighttime).

	Ebb tide daytime	Flood tide nighttime	Ebb tide nighttime
Temperature (°C)	30.3 ± 0.3 28.8 - 31.0	29.0 ± 0.7 28.1 - 30.0	27.6 ± 0.03 27.6 - 27.7
Salinity	0.38 ± 0.00 0.38 - 0.42	0.41 ± 0.02 0.39 - 0.44	0.72 ± 0.07 0.58 - 0.80
pCO_2 (ppmv)	7,439 ± 1,390 5,318 – 11,600	11,191 ± 2,264 7,366 - 13,919	18,276 ± 3,408 6,358 – 21,720
DIC (µmol kg-1)	1,105 ± 32 1,071 – 1,143	1,259 ± 77 1,103 - 1,335	2,213 ± 210 1,791 – 2,407
TA (µmol kg-1)	860 ± 36 805 - 912	931 ± 34 885 - 981	1,582 ± 169 1,246 – 1,749
pH (NBS)	7.06 ± 0.06 6.84 - 7.61	6.92 ± 0.10 6.81 - 7.07	6.89 ± 0.03 6.80 - 6.93
δ^{13}C-DIC (‰)	-4.10 ± 0.95 -6.00 to -3.27	-5.99 ± 1.12 -7.65 to -4.45	-8.57 ± 0.15 -8.79 to -8.28
Chl a (µmol kg-1)	66.7 ± 4.0 61.3 - 72.1	19.0 ± 3.4 15.5 - 22.4	-
DO (%sat)	59.8 ± 10.8 5.2 - 80.3	39.2 ± 14.2 23.9 - 62.0	4.9 ± 4.3 0.2 - 13.1

Table 3 Calculated mean values for gas exchange coefficient (k_{600}) and CO_2 fluxes at the air-water interface in each estuarine regions of the PSRE, as well as, the spatial time-integrated fluxes for the whole system. The periods M, A, and N represents the morning, afternoon and night. W92 is the data calculated according to k600 of Wanninkhof (1992), RC01 is the data calculated according to k600 of Raymond and Cole (2001), and A09 is data calculated according to k600 of Abril et al. (2009).

	Period	FCO_2 (mmol C m^{-2} d^{-1}) W92	FCO_2 (mmol C m^{-2} d^{-1}) RC01	FCO_2 (mmol C m^{-2} d^{-1}) A09	K_{600} (cm h^{-1}) W92	K_{600} (cm h^{-1}) RC01	K_{600} (cm h^{-1}) A09
Feb – 17							
0-5 (21.50 km^2)	M	-1.61	-7.44	-11.52	0.69	3.21	4.98
	A	-12.07	-18.46	-19.49	5.21	7.97	8.42
	N	-2.30	-8.18	-12.46	1.00	3.54	5.38
5-30 (49.00 km^2)	M	-0.34	-1.56	-2.78	0.69	3.21	5.76
	A	-2.52	-3.86	-5.11	5.21	7.97	10.56
	N	-0.48	-1.70	-3.05	1.00	3.54	6.32
> 30 (20.00 km^2)	M	0.38	1.75	3.14	0.69	3.21	5.76
	A	2.86	4.37	5.78	5.21	7.97	10.56
	N	0.55	1.94	3.46	1.00	3.54	6.32
Mangrove Creek (0.25 km^2)	M	1.97	28.56	34.92	0.17	2.47	3.02
	A	14.35	44.30	48.82	1.24	3.82	4.22
	N	2.88	30.07	41.18	0.25	2.6	3.56
All Estuary (90.75 km^2) are-averaged	M	-0.48	-2.14	-3.43			
	A	-3.55	-5.38	-5.98			
	N	-0.67	-2.35	-3.72			
		-1.34	**-3.05**	**-4.22**			
Oct – 17							
0-5 (12.90 km^2)	M	-5.64	-10.34	-12.86	3.17	5.82	7.23
	A	-26.23	-37.80	-21.55	14.75	21.26	12.12
	N	-9.26	-14.16	-14.98	5.21	7.97	8.42
5-30 (30.60 km^2)	M	-2.74	-5.04	-7.70	3.17	5.82	8.9
	A	-12.77	-18.41	-13.61	14.75	21.26	15.73
	N	-4.51	-6.91	-9.14	5.21	7.97	10.56
> 30 (47.00 km2)	M	0.12	0.22	0.34	3.17	5.82	8.9
	A	0.55	0.82	0.60	14.75	21.26	15.73
	N	0.19	0.31	0.41	5.21	7.97	10.56
Mangrove Creek (0.25 km^2)	M	23.09	107.40	131.16	0.69	3.21	3.92
	A	126.82	216.14	171.31	3.79	6.46	5.12
	N	41.50	127.80	141.19	1.24	3.82	4.22
All Estuary (90.75 km^2) area-averaged	M	-1.61	-2.76	-3.89			
	A	-7.39	-10.56	-6.86			
	N	-2.62	-3.84	-4.61			
		-3.55	**-5.26**	**-4.99**			
Mar – 18							
0-5 (21.50 km^2)	M	6.36	41.76	66.17	0.44	2.89	4.58
	A	68.06	107.35	117.77	4.71	7.43	8.15
	N	12.86	49.70	75.72	0.89	3.44	5.24
5-30 (62.00 km^2)	M	-0.12	-0.82	-1.49	0.44	2.89	5.21
	A	-1.34	-2.14	-2.93	4.71	7.43	10.19
	N	-0.26	-0.98	-1.75	0.89	3.44	6.13
> 30 (7.00 km^2)	M	0.05	0.36	0.65	0.44	2.89	5.21
	A	0.60	0.94	1.27	4.71	7.43	10.19
	N	0.12	0.43	0.77	0.89	3.44	6.13

Mangrove Creek (0.25 km^2)	M	9.34	198.72	219.84	0.11	2.34	3.38
	A	105.31	324.41	358.39	1.24	3.82	4.22
	N	26.33	228.46	289.08	0.31	2.69	3.63
All Estuary (90.75 km^2) area-averaged		1.46	9.91	15.50			
		15.55	24.94	26.98			
		2.95	11.76	17.64			
		5.71	**14.59**	**19.37**			

Table 4 Net Community Production (NCP) estimated for the mixing zone. The NCP was estimated as the difference between (ΔFCO_2), ($\Delta FCO_{2mixing\ corrected}$) and ($\Delta FCO_{2cooling/heating}$). FCO_2, $FCO_{2mixing\ corrected}$ and $FCO_{2cooling/heating}$ were calculated with the values of $pCO_{2measured}$, $pCO_{2mixing\ corrected}$ and $pCO_{2cooling/heating}$. See the section 3.55 in material and methods and 4.3 in discussion for further details.

	Mixing Zone
Feb – 17	
$\Delta FCO_2 = FCO_{2mixing} - FCO_2$ (mmol C m^{-2} d^{-1})	-2.18
$\Delta FCO_{2mixing\ corrected} = FCO_{2mixing} - FCO_{2mixing\ corrected}$ (mmol C m^{-2} d^{-1})	-0.18
$\Delta FCO_{2cooling/heating} = FCO_{2mixing} - FCO_{2cooling/heating}$ (mmol C m^{-2} d^{-1})	-0.30
$NCP = (\Delta FCO_2) - (\Delta FCO_{2mixing\ corrected}) - (\Delta FCO_{2cooling/heating})$	-1.70
Oct – 17	
$\Delta FCO_2 = FCO_{2mixing} - FCO_2$ (mmol C m^{-2} d^{-1})	-2.95
$\Delta FCO_{2mixing\ corrected} = FCO_{2mixing} - FCO_{2mixing\ corrected}$ (mmol C m^{-2} d^{-1})	-1.02
$\Delta FCO_{2cooling/heating} = FCO_{2mixing} - FCO_{2cooling/heating}$ (mmol C m^{-2} d^{-1})	-0.79
$NCP = (\Delta FCO_2) - (\Delta FCO_{2mixing\ corrected}) - (\Delta FCO_{2cooling/heating})$	-1.13
Mar – 18	
$\Delta FCO_2 = FCO_{2mixing} - FCO_2$ (mmol C m^{-2} d^{-1})	-0.46
$\Delta FCO_{2mixing\ corrected} = FCO_{2mixing} - FCO_{2mixing\ corrected}$ (mmol C m^{-2} d^{-1})	0.69
$\Delta FCO_{2cooling/heating} = FCO_{2mixing} - FCO_{2cooling/heating}$ (mmol C m^{-2} d^{-1})	-0.57
$NCP = (\Delta FCO_2) - (\Delta FCO_{2mixing\ corrected}) - (\Delta FCO_{2cooling/heating})$	-0.58

Figure Captions

Figure 1. Map 1a shows the localization of the state of Rio the Janeiro. The river basins are shown in shades of grey. Map 1b shows the localization of the PSRE and adjacent shelf waters. The colored lines represent the boat track with online and continuous measurements of pCO_2, DO, pH, temperature, and salinity. Note that the boat track varied in each sampling campaign: light green, dark green and blue represent Feb 17, Oct 17 and Mar-18, respectively. Along the boat track, discrete stations were sampled (the exact localization of the sampling stations exhibited variations between sampling campaigns according to the boat track and the salinity gradient). The yellow star represents the localization of the anchoring station (Eulerian time-series data). Graph c shows a comparison between the river water discharge for the year of sampling (2017/2018) and the historical average. The red arrows are the sampling months. Graph d shows a historical tendency of decreasing river flow (average monthly values).

Figure 2. Maps of continuous measurements of a) salinity, b) pH, c) DO, and d) pCO_2 in surface waters of the PSRE for all sampling campaigns.

Figure 3. Distribution of pCO_2 along the salinity gradient in the PSRE separated by sampling campaigns. Graphs a), c), e) and g) include all the data, with the main estuarine channel and the mangrove creek. Graphs b), d), f) and h) include only the data in the main estuarine channel.

Figure 4. Distributions of TA, DIC, δ^{13}C-DIC, and Chl *a* in discrete samples along the salinity gradient. The black dots are the main estuarine channel and the green dots are the mangrove creek. The dashed blue lines represent the theoretical models of conservative mixing endmembers.

Figure 5. Relationship between the concentrations of Chl *a vs*. pCO_2 along the main channel of the PSRE. The different symbols in the figure represent the sampling campaigns, as indicated in the caption. The terms “river” and “ocean” represent the values found in the river and ocean endmembers, respectively, for the different sampling campaigns.

Figure 6. Eulerian time-series data of the mangrove creek. The shaded area symbolizes the nighttime sampling.

Figure 7. Scatter plots between a) TA or DIC and salinity, b) TA and DO, c) δ^{13}C-DIC and DO, d) δ^{13}C-DIC and pCO_2 in the mangrove creek throughout the 20 h cycle on Mar 18. Red dots characterize hypoxic condition with DO_{sat}% <25% observed in early morning and low tide.

Figure 8. Graph a shows the relationship between the excess dissolved inorganic carbon (E-DIC) and apparent oxygen utilization (AOU) in the PSRE main channel and mangrove creek for the three sampling campaigns. Green dots are the stations in the mangrove creek and blue dots are the stations in the main estuarine channel. The 1:1 line represents the quotient between CO_2 and O_2 during the processes of photosynthesis and respiration. Graph b) shows the deviations from conservative mixing

lines of total alkalinity (ΔTA) as a function of dissolved inorganic carbon (ΔDIC), including the three sampling campaigns. Green dots are the stations in the mangrove creek and blue dots are the stations in the main estuarine channel. α indicates the slope of the linear regression line.

Figure 9. Comparison between mixing model and $pCO_{2\ measured}$ in the mixing zone, including corrections performed for gas exchange and thermal variability and deviations from the conservative mixing. Graphs a), c) and e) show the means and standard deviations of $pCO_{2\ measured}$ (black dots), $pCO_{2\ mixing}$ (blue dots), $pCO_{2\ gas\ exchange}$ (green dots) and $pCO_{2\ cooling/heating}$ (red dots) for each salinity unit. Graphs b), d) and f) show the difference between $pCO_{2\ measured}$ and $pCO_{2\ mixing}$ ($\Delta pCO_{2\ measured}$), $pCO_{2\ gas\ exchange}$ and $pCO_{2\ mixing}$ ($\Delta pCO_{2\ gas\ exchange}$), and the cumulative difference between $pCO_{2\ gas\ exchange} + pCO_{2\ cooling/heating}$ and $pCO_{2\ mixing}$ ($\Delta pCO_{2\ gas\ exchange\ +\ cooling/heating}$). The green arrow indicates the effect of gas exchange compared with $pCO_{2\ mixing}$ (influx or efflux of CO_2). The red arrow indicates the effect of thermal variability (cooling and heating). The grey arrow indicates the residual difference between $pCO_{2\ measured}$ and $pCO_{2\ mixing}$ attributed to biological activities.

Figure 10. Deviations from conservative mixing lines of stable isotope composition of DIC ($\Delta\delta^{13}$C-DIC) as a function of DIC (ΔDIC) for the main channel. Different colors represent the sampling campaigns. The origin represents the conservative mixing with sample values equal to the ocean endmember value. The four quadrants (PP/OG, CP, DC, and CD) in the graph indicate the processes that could influence the DIC and δ^{13}C-DIC distributions. Quadrant PP/OG represents the primary production/outgassing of CO_2, when DIC concentrations increase and δ^{13}C-DIC values decrease. Quadrant CP represents the carbonate precipitation, when DIC concentrations and δ^{13}C-DIC values decrease. Quadrant DC represents the degradation of organic carbon, when DIC concentrations increase and δ^{13}C-DIC decrease. Quadrant CD represents the carbonate dissolution, when the DIC concentrations and δ^{13}C-DIC values increase. The red vectors represent the slopes of specific processes affecting the DIC and δ^{13}C-DIC distributions: primary production (slope = -24.0‰), CO_2 outgassing (slope = -8.4‰), and organic carbon degradation using the δ^{13}C-DIC value of river water (-16.0‰). The grey arrows represent the direction that the samples will follow if they are subject to more than one process (organic matter degradation followed by primary production, which is drawn parallel to vector of primary production; and organic carbon degradation followed by CO_2 outgassing, which is drawn parallel to the vector of CO_2 outgassing). Details about the formulations and calculations of these vectors can be found in Alling et al. (2012), Samanta et al. (2015), and Cotovicz Jr. et al. (2019).

Figure 1

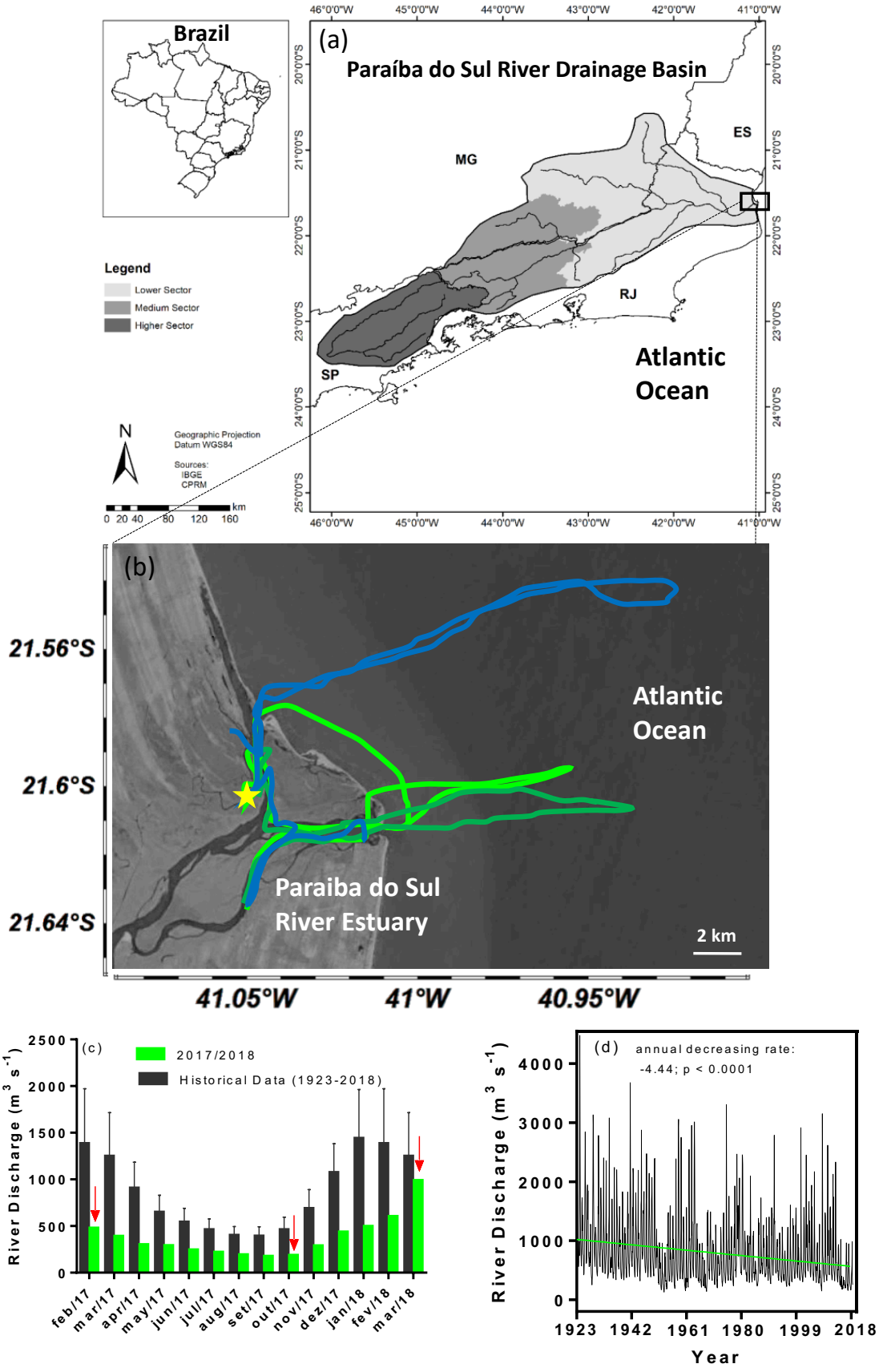
Brazil
(a)
Paraíba do Sul River Drainage Basin
MG
ES
RJ
SP
Atlantic Ocean
Legend
Lower Sector
Medium Sector
Higher Sector
N
Geographic Projection
Datum WGS84
Sources:
IBGE
CPRM
0 20 40 80 120 160 km
46°0'0"W
45°0'0"W
44°0'0"W
43°0'0"W
42°0'0"W
41°0'0"W
20°0'0"S
21°0'0"S
22°0'0"S
23°0'0"S
24°0'0"S
25°0'0"S
(b)
21.56°S
21.6°S
21.64°S
Atlantic Ocean
Paraiba do Sul River Estuary
2 km
41.05°W
41°W
40.95°W
(c)
2017/2018
Historical Data (1923-2018)
River Discharge (m3 s-1)
2500
2000
1500
1000
500
0
feb/17
mar/17
apr/17
may/17
jun/17
jul/17
aug/17
set/17
out/17
nov/17
dez/17
jan/18
fev/18
mar/18
(d)
annual decreasing rate:
-4.44; p < 0.0001
River Discharge (m3 s-1)
4000
3000
2000
1000
0
1923
1942
1961
1980
1999
2018
Year

Figure 2

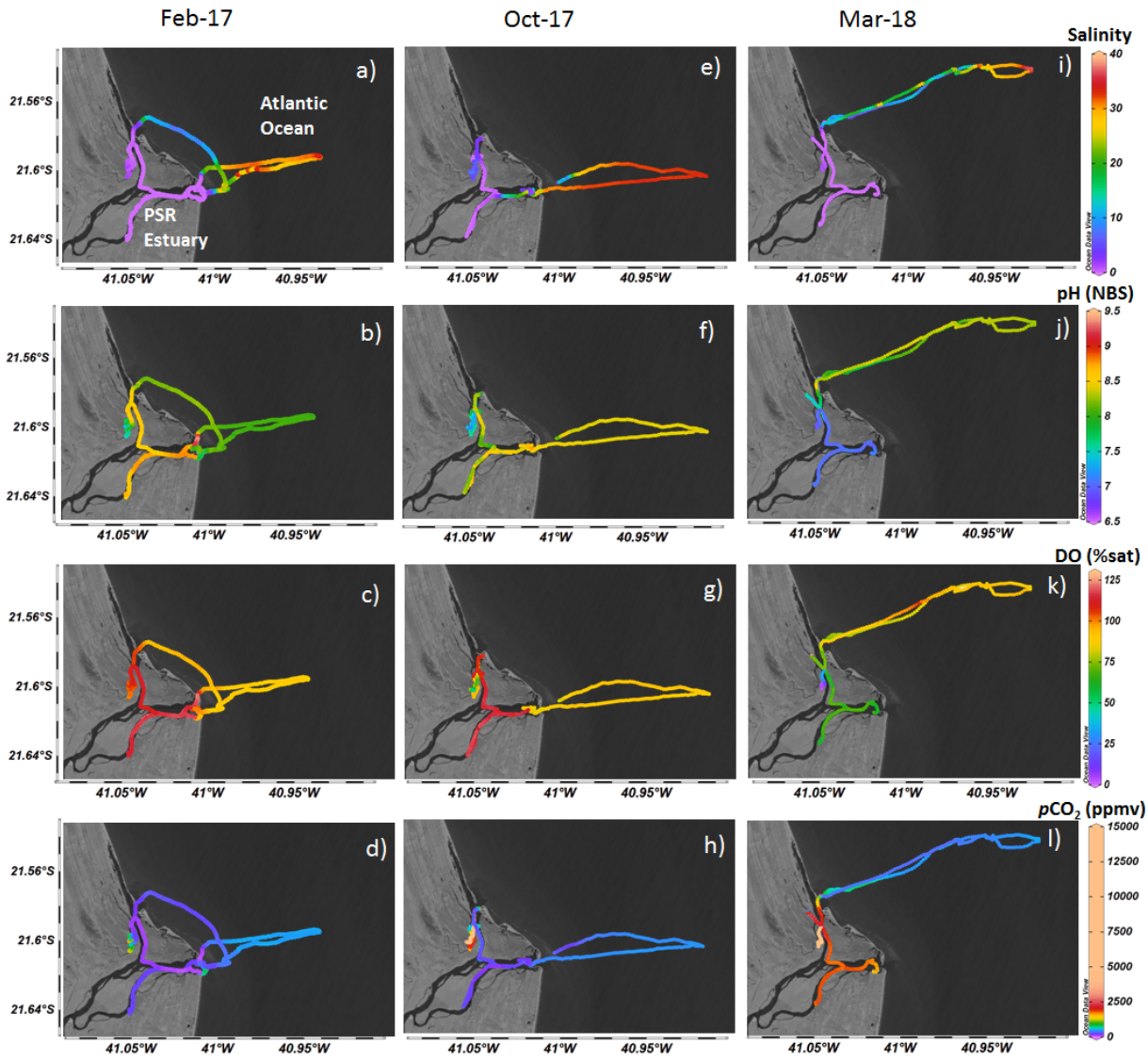
Feb-17
Oct-17
Mar-18
Salinity
pH (NBS)
DO (%sat)
pCO2 (ppmv)
a)
b)
c)
d)
e)
f)
g)
h)
i)
j)
k)
l)
Atlantic Ocean
PSR Estuary
21.56°S
21.6°S
21.64°S
41.05°W
41°W
40.95°W
40
30
20
10
0
9.5
9
8.5
8
7.5
7
6.5
125
100
75
50
25
0
15000
12500
10000
7500
5000
2500
0

Figure 3

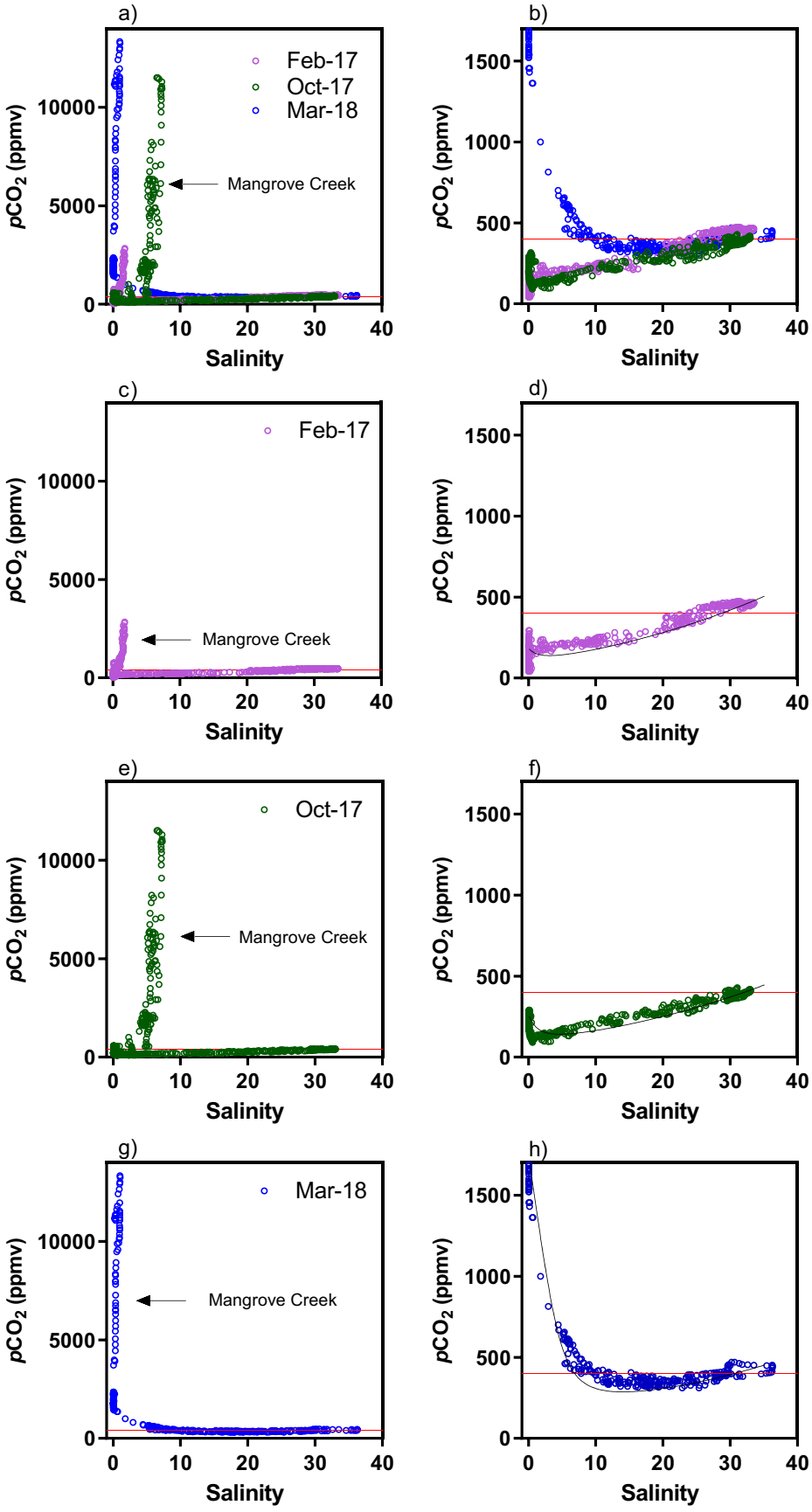
a)
b)
c)
d)
e)
f)
g)
h)
Feb-17
Oct-17
Mar-18
Mangrove Creek
pCO2 (ppmv)
Salinity
0
5000
10000
500
1000
1500
10
20
30
40

Figure 4

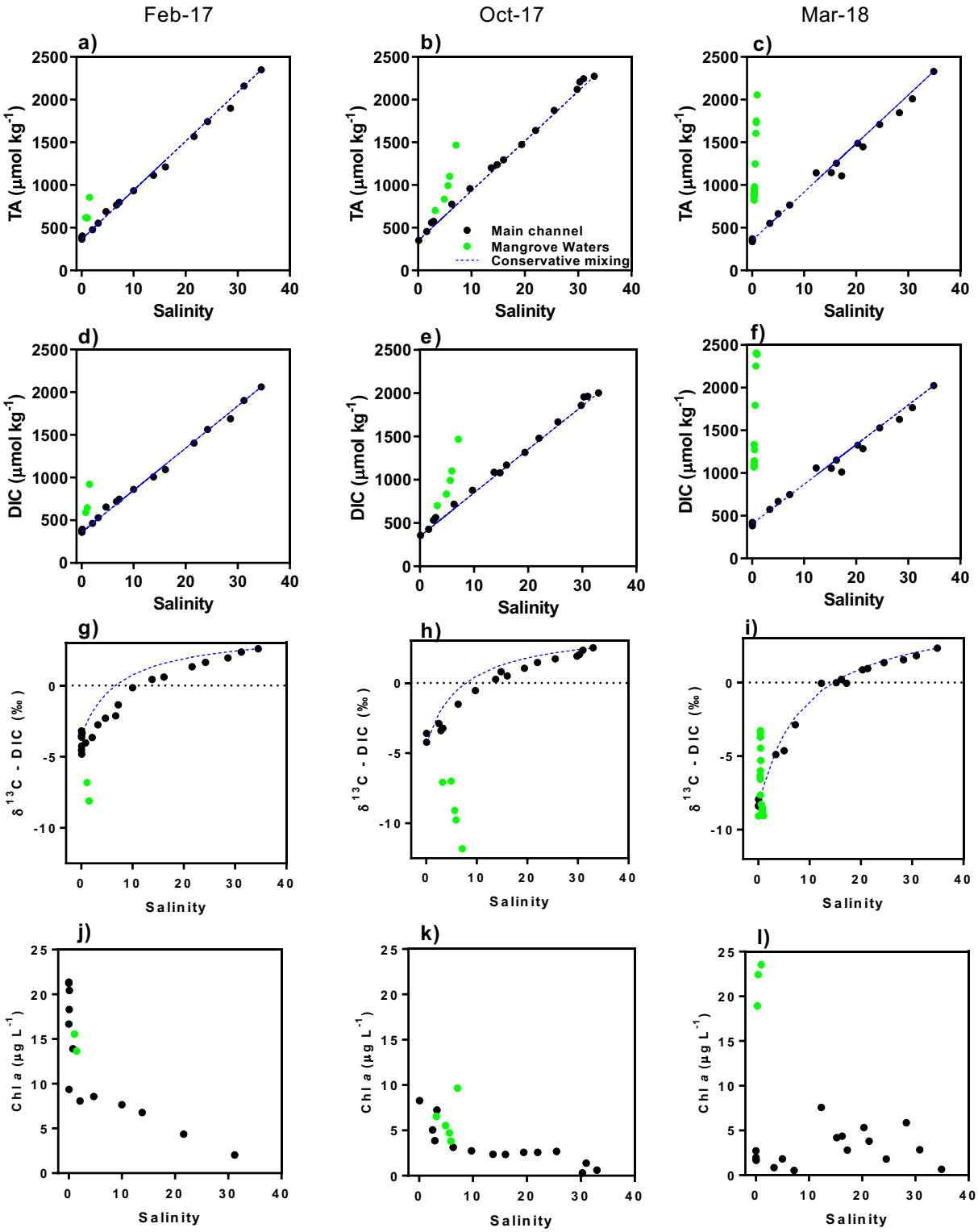
Feb-17
Oct-17
Mar-18
a)
b)
c)
d)
e)
f)
g)
h)
i)
j)
k)
l)
TA (µmol kg-1)
DIC (µmol kg-1)
δ13C - DIC (‰)
Chl a (µg L-1)
Salinity
Main channel
Mangrove Waters
Conservative mixing

Figure 5

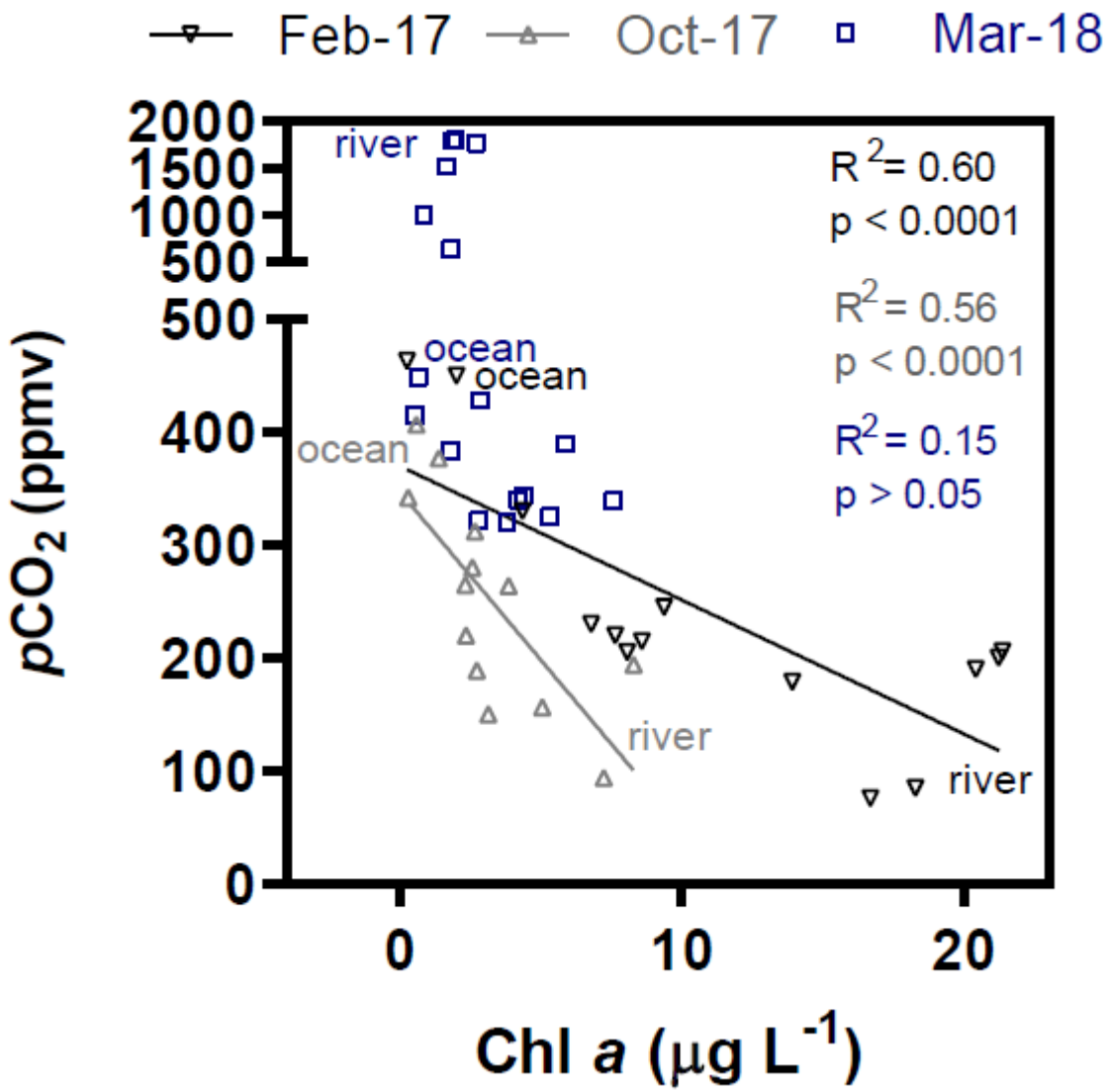

Figure 6

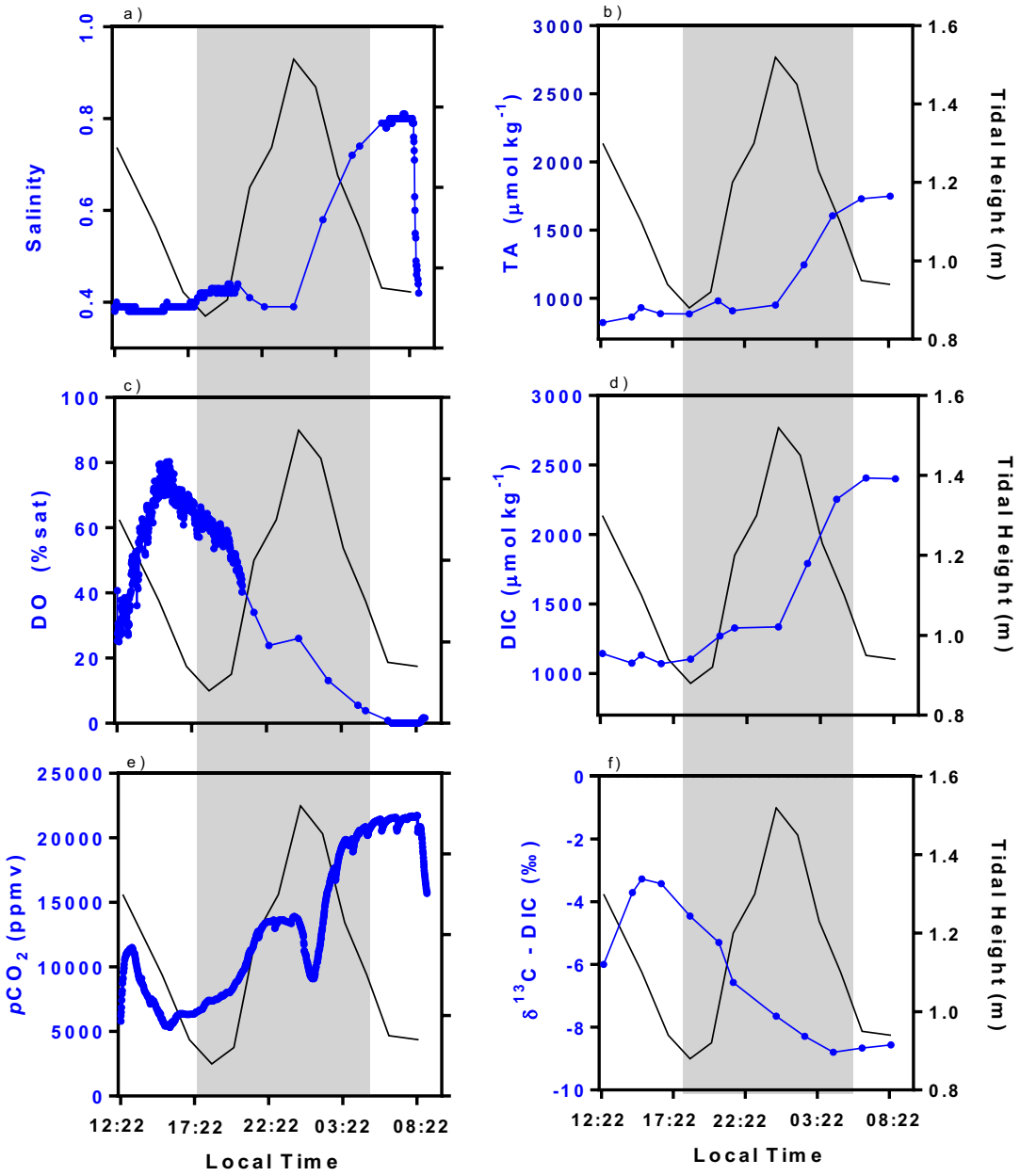
a)
Salinity
0.4
0.6
0.8
1.0
b)
TA (µmol kg-1)
1000
1500
2000
2500
3000
Tidal Height (m)
0.8
1.0
1.2
1.4
1.6
c)
DO (%sat)
0
20
40
60
80
100
d)
DIC (µmol kg-1)
e)
pCO2 (ppmv)
0
5000
10000
15000
20000
25000
f)
δ13C - DIC (‰)
-10
-8
-6
-4
-2
0
12:22
17:22
22:22
03:22
08:22
Local Time

Figure 7

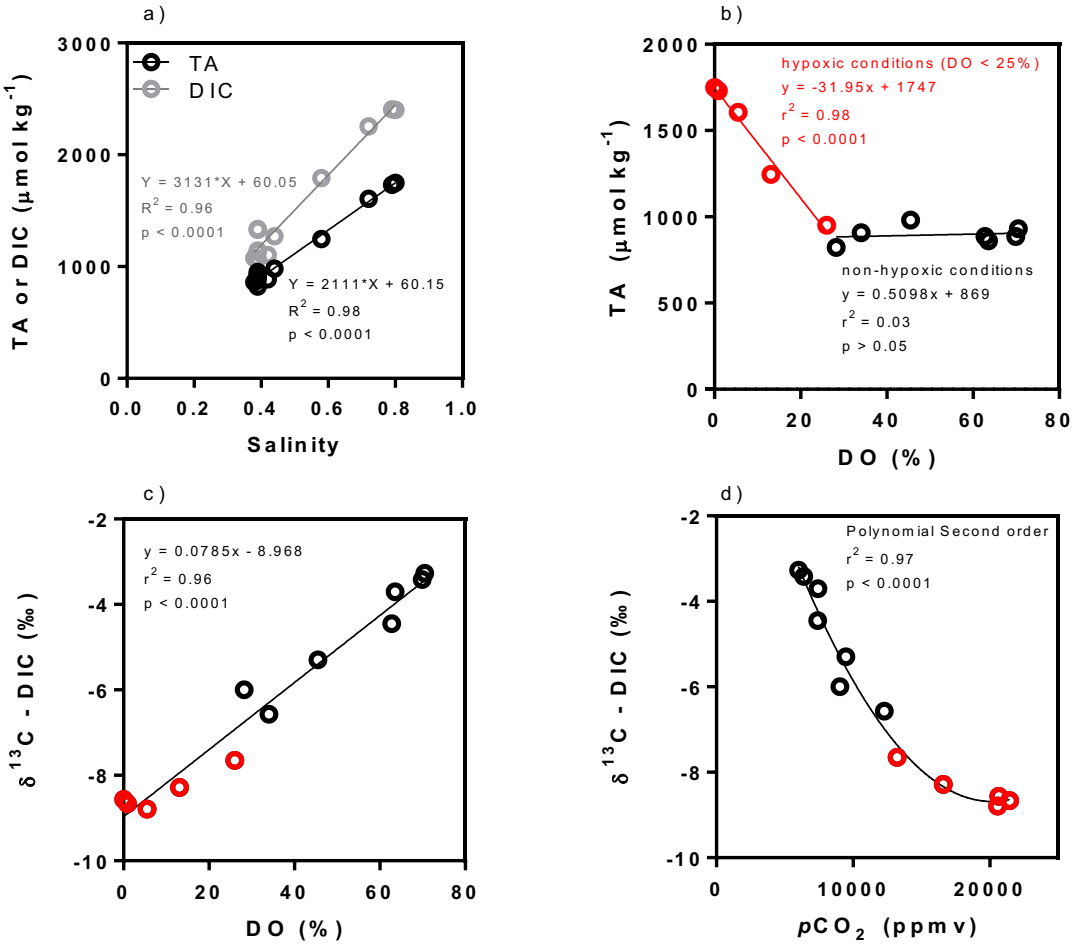
a)
TA
DIC
Y = 3131*X + 60.05
R2 = 0.96
p < 0.0001
Y = 2111*X + 60.15
R2 = 0.98
p < 0.0001
TA or DIC (µmol kg-1)
Salinity
b)
hypoxic conditions (DO < 25%)
y = -31.95x + 1747
r2 = 0.98
p < 0.0001
non-hypoxic conditions
y = 0.5098x + 869
r2 = 0.03
p > 0.05
TA (µmol kg-1)
DO (%)
c)
y = 0.0785x - 8.968
r2 = 0.96
p < 0.0001
δ13C - DIC (‰)
DO (%)
d)
Polynomial Second order
r2 = 0.97
p < 0.0001
δ13C - DIC (‰)
pCO2 (ppmv)

Figure 8

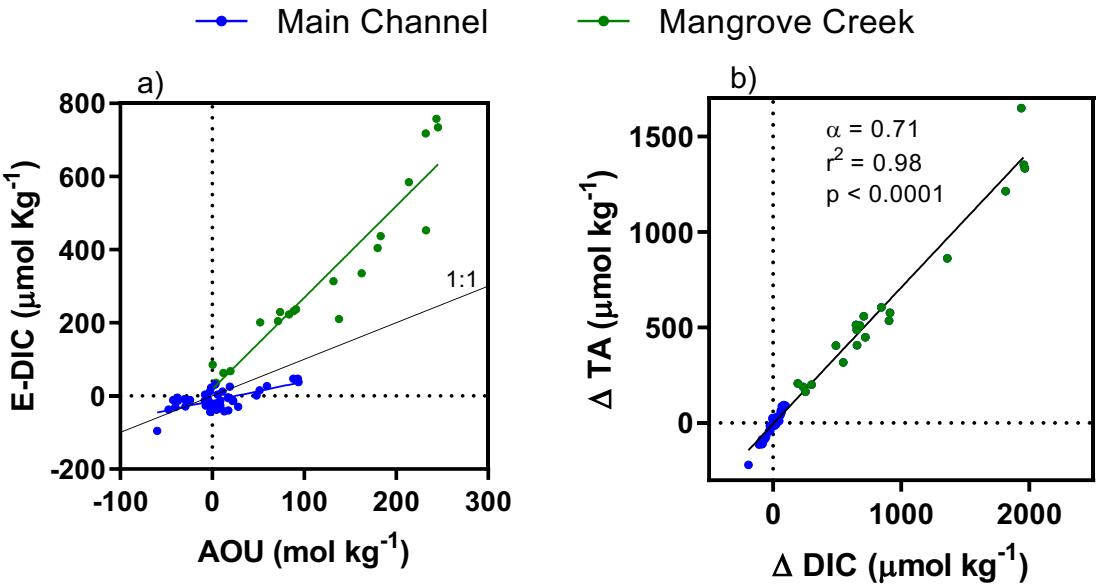
Main Channel
Mangrove Creek
a)
E-DIC (µmol Kg-1)
AOU (mol kg-1)
1:1
b)
Δ TA (µmol kg-1)
Δ DIC (µmol kg-1)
α = 0.71
r2 = 0.98
p < 0.0001

Figure 9

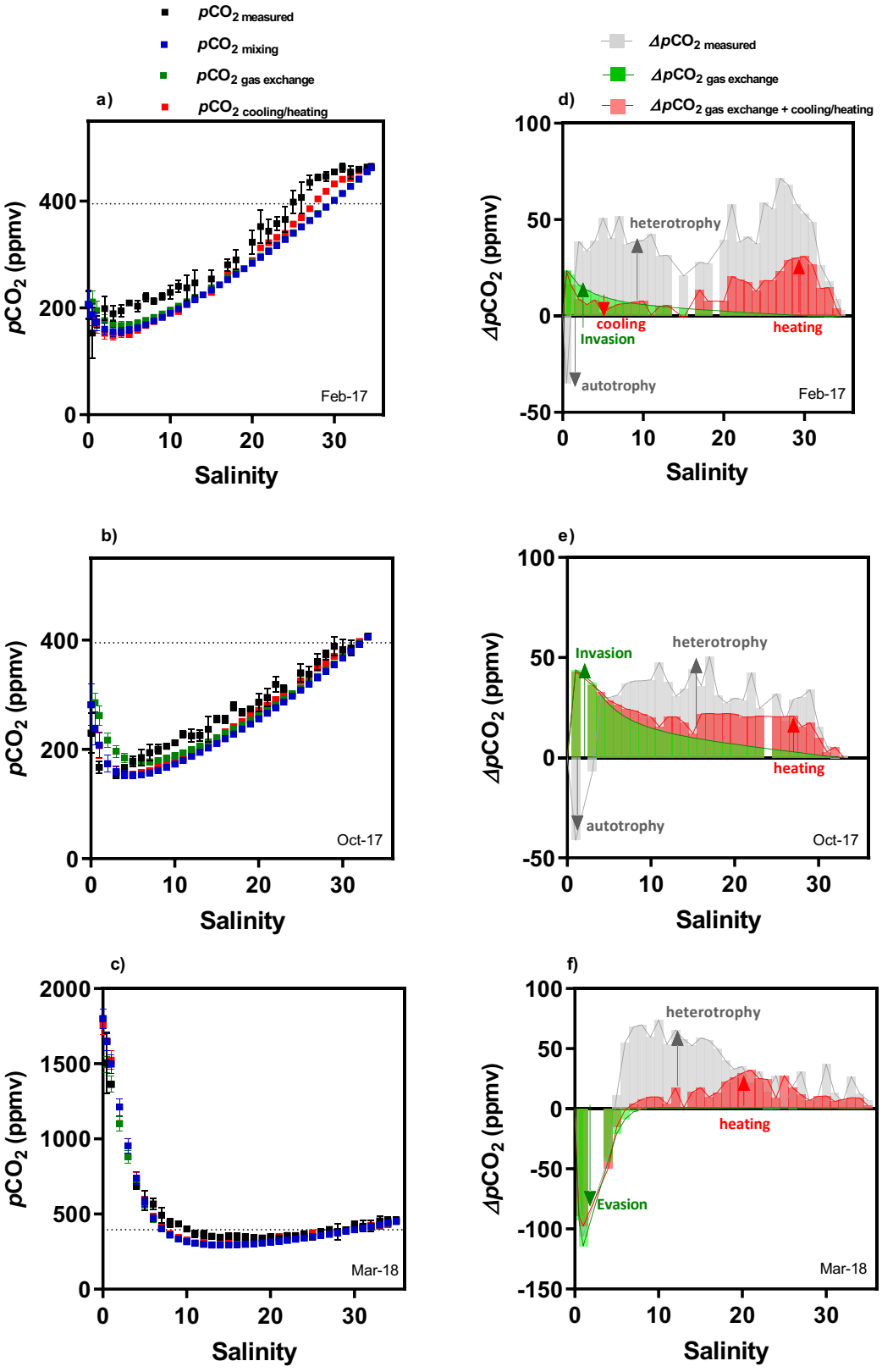
a)
pCO_2 measured
pCO_2 mixing
pCO_2 gas exchange
pCO_2 cooling/heating
pCO_2 (ppmv)
Salinity
Feb-17
b)
Oct-17
c)
Mar-18
d)
ΔpCO_2 measured
ΔpCO_2 gas exchange
ΔpCO_2 gas exchange + cooling/heating
ΔpCO_2 (ppmv)
heterotrophy
cooling
Invasion
heating
autotrophy
e)
f)
Evasion

Figure 10

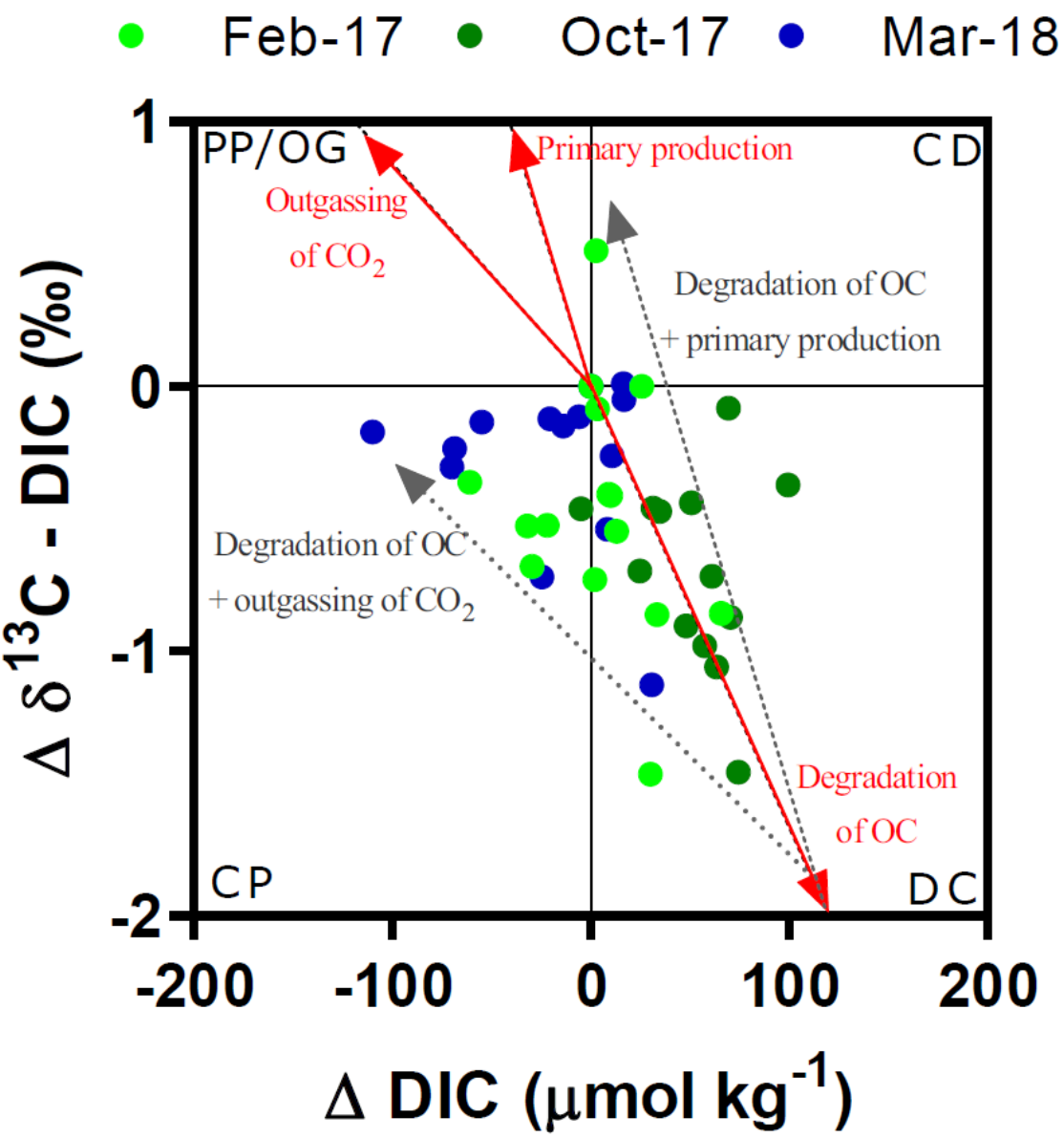
Feb-17
Oct-17
Mar-18
PP/OG
Primary production
CD
Outgassing
of CO2
Degradation of OC
+ primary production
Degradation of OC
+ outgassing of CO2
Degradation
of OC
CP
DC
1
0
-1
-2
-200
-100
0
100
200
Δ δ13C - DIC (‰)
Δ DIC (μmol kg-1)